A DENSITY FUNCTIONAL THEORY GUIDE TO HIGH QUALITY MODIFICATION OF MIXED METAL OXIDES USED FOR PHOTOCATALYTIC WATER SPLITTING

by

CEDRIC LEON MAYFIELD

Presented to the Faculty of the Graduate School of
The University of Texas at Arlington in Partial Fulfillment
of the Requirements
for the Degree of

DOCTOR OF PHILOSOPHY

THE UNIVERSITY OF TEXAS AT ARLINGTON
December 2015

Copyright © by Cedric Mayfield 2015

All Rights Reserved

Acknowledgements

I would like to thank my advisor Professor Muhammad Huda for inviting me to join his condensed matter theory group, and giving me the opportunity to do research in the exciting field of solar energy conversion materials. The current work would not have been possible without his patience, guidance, and encouragement. His genuine passion for science and insightful words on research related issues are inspiring to me. Dr. Huda has been the perfect example of how to be a scientist that works with high standards and integrity. I am grateful for the time he has invested toward my development as a physicist. I am also grateful for his generous care and many discussions about life in general.

I would like to thank my committee members, Professor Alexander Weiss, Professor Raymond Lopez, Professor Qiming Zhang, and Professor Suresh Sharma for their support. I am thankful to have had the late Professor Asok Ray as my “grand-mentor” as he was like the “grand-father” of our research group. I am thankful to Ms. Angela Winters and Ms. Stacey Cody, for their diligence with administrative support. I would also like to thank Dr. Brenda Davis and Ms. Lisa Berry for keeping me connected with the CIRTL network and other graduate student resources over in the Office of Graduate Studies.

I would also like to acknowledge my group mates, Pranab Sarker, Prashant Khatri, Dr. Sarah Hernandez, Shafaq Moten, Sajib Barman, and Edan Bainglass. I find myself very lucky to have been among a diverse group of promising young physicists.

Last but not least I would like to thank the National Science Foundation and the National Renewable Energy Laboratory for their support.

November 10, 2015

Abstract

A DENSITY FUNCTIONAL THEORY GUIDE TO HIGH QUALITY MODIFICATION OF MIXED METAL OXIDES USED FOR PHOTOCATALYTIC WATER SPLITTING

Cedric Leon Mayfield, PhD

The University of Texas at Arlington, 2015

Supervising Professor: Muhammad N. Huda

Phase stability and charge transport of pristine and transition metal alloyed bismuth titanate ($Bi_2Ti_2O_7$, a.k.a. BTO), a photocatalytic water splitter, has been studied using the generalized gradient approximated density functional theory (GGA-DFT). The primary goals of this work were to predict the effective conditions for pure phase synthesis of the modified ternary multi-metal oxide and to determine the most suitable modifications for enhancing its photocatalytic properties. To understand the details of phase stability and photoconduction, we have derived the formation enthalpies, defect formation energies, electronic structures, spectral absorptions and polaron activation energies for pristine and transition metal doped bismuth titanate ($Bi_2Ti_2O_7$, a.k.a. BTO). Implantation of the localized 3d electrons is a primary band engineering technique for extending the spectral absorptions of metal oxides into the visible range. However, localized states typically increase charge trapping that reduces crucial photocurrent for the photocatalytic process. Therefore one objective here is to understand the extent to which localization plays a role in electron transfer and which mode of conduction, band or polaron hopping, is dominantly effected.

As predicting the effective conditions for pure phase stability and modeling electron transport of multi metal oxide materials is still in development as a whole, we

have benchmarked our methods by reproducing relative quantities of world class metal oxide photocatalyst, rutile TiO_2 and monoclinic scheelite $BiVO_4$. In recognition of our methods, our results have been used to enhance H_2 production of a facile hydrothermal synthesized Fe-doped BTO. Furthermore, we demonstrate with results for Cr- and Mn-doped BTO how experimental characterization can also be enhanced.

For each transition metal ion (M = Cr, Mn, and Fe), pure phase stability has a unique association with the presence or absence of O defects. Band modifications vary with impurity d electron configuration and the polaron activation energies are increased with accompanying oxygen interstitials or vacancies. Hence, the ideal doping promotes the desired band gap reduction while maintaining the underlying stoichiometry. Thus, the key mechanism for phase stability and optimized photocurrent is the O chemical potential which is limited by dopant inspired phases (DIPs) instead of the host material.

Table of Contents

List of Illustrations

List of Tables

Chapter 1

Introduction

1.1 Opposition to a Global Threat

The Natural Resources Defense Council has stated climate change is our greatest environmental threat. Climate change encompasses the rising seas, raging storms, searing heat, ferocious fires, severe drought and punishing floods [1–4] we have experienced commonly in 2015. It is a result of concentrated atmospheric carbon that has created a radiative barrier around our planet preventing reflected heat from escaping into space [5]. This trapped heat has already begun melting our polar ice caps; raising sea levels, altering ocean and wind currents, etc. [6]. In the United States alone, electric power plants emit about 2.2 billion tons of CO_2 each year [7]. Clearly then, fossil fuel as an energy source has surpassed its point of diminishing returns and the need for alternative energy sources are immediate.

The most viable state of the art technologies called upon to pacify this global threat such as wind turbine technologies and photovoltaic cells have emerged and commercialized but at an operational cost inadequate for the label of a sustainable resource [8]. Solar flux varies on the surface of the planet so the opportunity to harness solar energy is discontinuous. This presents a challenge for storing energy for nighttime use. Here we have taken a focus on photocatalytic water splitting for the conversion of solar energy into chemical energy. Photocatalytic water splitting is an environmentally benign way to produce the volatile fuels, hydrogen and oxygen gas [9]. Both of these fuels are clean fuels and thus, potentially contribute to the reduction of global carbon emissions. Also in the form of water hydrogen and oxygen gas are ideally stored; safely and inactive. However, there are still challenges in this field which encompasses the design of materials that can be activated with lower energy photons.

The most functional and tunable materials used as photocatalysts are mixed metal oxides. Mixed-metal oxides are a class of wide band gap semiconductors that typically cannot be activated by visible light and have low quantum efficiencies [10]. However these materials possess the tunability required to overcome the challenges via selective modifications. In this dissertation selective modifications refer to chemical compositional changes of the electronic structure intended to optimize the primary components of the photocatalytic process. For example, in titania based oxides, it is possible to create mixed bands by mixing transition metal orbitals with O 2p orbitals lowering the host band gap. Therefore our focus is on doping a ternary metal oxide and the effects on its phase stability and photoconduction.

Discussion of several methods developed within the scope of density functional theory are provided in detail. We discuss the relevance of our study in the context of metal oxide synthesis. We also discuss the key issues associated with treatment of the semi-local nature of DFT. Ultimately we show a theoretical toolset that should accompany synthesis of every modified mixed metal oxide. The guidance provided by our theoretical/computational method has resulted in higher quality synthesis of Fe-doped BTO. We also benchmarked our method by reproducing well known results of the well-known materials, all of which were thoroughly assessed and characterized by our methods to gain insights about various phase stabilities, chemical compositions, light absorptions, and charge transport properties.

Solar energy conversion can potentially satisfy the world’s increasing energy demand, maintain its effectiveness through climate change, and contribute to the reduction of carbon emissions. Our prototype, $Bi_2Ti_2O_7$ (BTO), a photocatalyst for water splitting, can be enhanced by cation substitution to absorb photons with energies in the visible range. From a theoretical standpoint, simply introducing one or two transition metal (TM) atoms per unit cell of BTO can reduce the band gap sufficiently enough to absorb visible light, but from the experimental standpoint, stabilizing two and three cations of different valence is a formidable task. O defects often result when substituting cations of different valence. The emerging configurational variance ($Bi_{2-x}TM_xTi_2O_{7\pm y}$ and $Bi_2Ti_{2-x}TM_xO_{7\pm y}$) interrupts structure stability and leads to the formation of secondary phases. Also, material challenges involving the limitations of electron transfer in mixed metal oxides is important to understand in order to increase current solar to hydrogen (STH) efficiencies. In oxides charge trapping occurs where an electron is localized to a lattice site and can only be diffused by thermal excitations. The nuclear rearrangements associated with thermal excitation ultimately release the electron from its trapped state, however the activation barrier energies are seldom explored. Therefore we also investigate the activation energies of small polarons in BTO.

1.2 Photocatalytic Water Splitting, Solar Energy Storage and Conversion

Plant photosynthesis produces oxygen and hydrogen. The oxygen is released into the atmosphere for us and the hydrogen is combined with carbon dioxide to make carbohydrates for the plant [11]. The respective processes are described by the following:

$$2H_2O_{(l)} \overset{h\nu}{\rightarrow} O_2 + 2H_2 \tag{1.1}$$

$$2nC0_2 + 2nH_2O \overset{h\nu}{\rightarrow} 2(CH_2O)_n + 2nO_2 \tag{1.2}$$

Photocatalyst research aims to mimick photosynthesis in order to produce oxygen and hydrogen. The way to do so is through the overall water splitting reaction. Overall water splitting is comprised of the following two half reactions:

$$4H^+ + 4e^- \rightarrow 2H_2 \tag{1.3}$$

$$O_2 + 4H^+ + 4e^- \rightarrow H_2O \tag{1.4}$$

where protons are reduced to evolve hydrogen gas (equation 1.3), and water is oxidized to evolve oxygen gas (equation 1.4). The water oxidation reaction requires four electrons and four protons so it is slightly more complex. Hence, the overall reaction (equation 1.1) is thermodynamically uphill, requiring 474 kJ/mol for the $4e^-$ process. In addition to this positive free energy requirement, there is typically an an extra 600 mV needed to overcome slow kinetics. Photocatalysts provide a means to drive overall water splitting in the forward direction. Visible light possesses enough energy to provide the free energy and allows the reaction to occur from an excited state with a lower activation barrier.

Photochemical water splitting was introduced by Fujishima and Honda in 1972 when they first reported the utility rate of rutile TiO_2 capable of water splitting under UV irradiation [12]. It was shown that in the presence of Fe^{3+}, photocurrent increased a few mA. As such significant worldwide research efforts have focused on improving the efficiency of semiconductor systems; either band modifications through doping or alloying. In either case, only basic requirements are needed for semiconductor photocatalyst.

1.3 Properties of the Ideal Photocatalyst

The photocatalytic properties of a semiconductor depend on its electronic structure. In the ideal semiconductor photocatalyst, as illustrated in figure 1.1, absorption of light higher in energy than the material’s band gap creates an electron/hole pair, where electrons are excited from the valence band (VB) to the conduction band (CB), leaving holes behind in the VB.

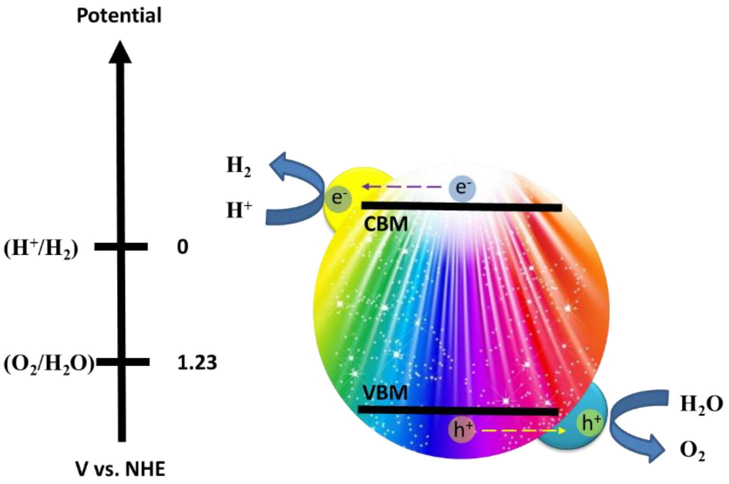

Figure 1.1 A schematic representation showing the key features of an ideal photocatalyst. The band edges straddle the redox potentials of water. The band gap accommodates absorption of visible light. Photo-excited charge carriers migrate to the surface, and both fuels hydrogen and oxygen gas evolve.

In order to maximize spectral absorption in the visible range, the band gap should be around 2 eV, which corresponds to absorption of wavelengths in the visible range of the electromagnetic spectrum. Traditionally, many wide band gap semiconductors, such as TiO_2 [13–17] and $SrTiO_3$ [18–23], have been explored as water splitting photocatalyst but their efficiencies are limited by large band gaps$(\geq 3.0 \text{ eV})$ in the UV range.

The solar flux density in the UV and visible regions of the solar spectrum are quite different. The solar spectrum is composed of 2% UV whereas visible light composes about 47%. Increasing the absorption of photocatalysts into the visble range of light has been the subject of much research in the recent years. However the methods for modifying oxide photocatalysts isn’t trivial as will be discussed throughout the context of this dissertation.

When optimizing a materials overall water splitting ability, the band edges should straddle the water splitting half reactions, as illustrated in figure 1.1. Upon the creation of photogenerated electron/hole pairs, the electrons and holes must be at sufficient energies to facilitate both half reactions. The CB should be at an energy more negative than the proton reduction potential (0 V vs NHE under standard conditions), and the VB should be more positive than the water oxidation potential (1.23 V vs NHE under standard conditions) in order to evolve both hydrogen and oxygen gas simultaneously.

Furthermore, the photogenerated charge-carriers should easily migrate to the surface without too much electron/hole pair recombination. High quality crystalline materials are attractive for suppressing recombination simply because fewer defects exists in high symmetry crystalline structures. For example intrinsic defects such as O_{vac} and O_{int} often occur due to the charge compensation mechanism of metal oxides, that can trap electrons and decrease photoactivity.

At last, the material must be inert. There are many attractive candidates with narrow band gaps for the overall water splitting reaction, however, their stability limits their usage, for example, compounds such as CdS and WO_3. The degradation of these catalysts is caused by photogenerated holes that decompose the compound. For example, WO_3 metal oxides are targeted on account of their abundance, affordability, and robustness. However, when efforts to design narrow band gap metal oxides include nitrogen substitution for oxygen, the compound break down. Nitrogen is decomposed by the photogenerated holes as follows:

$$\mathrm{2N^{3-} + 6h^{+} \rightarrow N_2} \qquad (1.5)$$

which is an evolution of nitrogen gas. More effective means of modification are discussed here in their relevant sections.

Chapter 2

Theory

2.1 Density Functional Theory

Density functional theory (DFT) is widely used for solving the many body quantum mechanical problems that arise in condensed matter physics and quantum chemistry. In 1964 it was shown by Hohenberg and Kohn that there is a one-to-one correspondence between the charge density of a system and the external potential that acts upon it [24]. Thereby the density that minimizes the total energy is the exact ground state density. As such, all properties of a chemical system's ground state can be derived from its single charge density instead of many charge particle wave functions. In principle, DFT is an 'exact' theory, applicable to any system in the presence of an external potential. In practice however, the accuracy of DFT depends on the representability of electronic exchange and correlation energies. Therefore approximated representations are introduced via an exchange-correlation (XC) functional, which also take into account the kinetic energy difference between the interacting (real) and the non-interacting (fictitious) systems. Over the years approximations made for the representability of electronic exchange and correlation, coupled with the technological advancements in computer architecture, have increased the predictability and accuracy of DFT computations significantly. In the following sections we will provide the reader with a concise introduction of the DFT framework following the reviews of Yang and Parr [25], Capelle [26] and Nagy [27]. The more specific methods used in this thesis will be addressed in their corresponding chapters.

2.2 The Hohenberg-Kohn Theorems

If a system of N electrons is under the influence of a time-independent external potential, $\mathrm{v}(\vec{\mathrm{r}})$, the Hohenberg-Kohn theorem states, $\mathrm{v}(\vec{\mathrm{r}})$ can be determined within an additive constant by just the electron density $\rho(\vec{r})$. In the first theorem [24] by Hohenberg and Kohn they cleverly showed this one-to-one correspondence via reductio ad absurdum proof which proceeds as follows. Suppose that in addition to $v(\vec{r})$ there exists a different potential $v'(\vec{r})$ that also corresponds to $\rho(\vec{r})$.This would imply that two ground state wave functions Ψ and Ψ' and to two different Hamiltonians H and H' and two different ground state energies E_0 and E'_0 are interchangeable. Then by invoking the Born-Oppenheimer approximation as it is routinely done for N electron systems, we obtain our Hamiltonians which are purely electronic.

$$H = -\frac{1}{2}\sum_{i}^{N} \nabla_i^2 + \sum_{i<j}^{N} \frac{1}{r_{ij}} + \sum_{i}^{N} v(\vec{r}) \tag{2.1}$$

In this electronic Hamiltonian the first and second terms represent the kinetic and electron-electron repulsion energies, respectively. The third term represents the accumulation of energy from each electron interacting with an external potential. Here we have used atomic units (a.u.), where one a.u. is equivalent to 27.212 eV. All distances are in units of Bohr radius (e.g. a_0 = 0.529 Å) and the square of electric charge e^2, Planck's constant $\hbar$, and electron mass m_e, are all considered to be unity.

Now by a process known as the variational method of quantum mechanics, we can say each of the lowest energy eigenstates should be discoverable. For this to indeed be the case within the Hohenberg-Kohn theorem, two similar but different perspectives should be coexistent. The first perspective is described by equation (2.2), which states, the expectation value of H operating on its ground state wave function Ψ should be lower in energy than the expectation value of H operating on any other wave function, including Ψ'.

$$\mathrm{E_0} = \langle\Psi|\mathrm{H}|\Psi\rangle < \langle\Psi'|\mathrm{H}|\Psi'\rangle = \langle\Psi'|\mathrm{H}|\Psi'\rangle + \langle\Psi'|\mathrm{H}-\mathrm{H}'|\Psi'\rangle \tag{2.2}$$
$$= \mathrm{E}_0' + \int \rho(\vec{\mathrm{r}})\,[\mathrm{v}(\vec{\mathrm{r}}) - \mathrm{v}'(\vec{\mathrm{r}})]\mathrm{d}\vec{\mathrm{r}}$$

The second perspective is described by equation 2.3, which states the expectation value of H' operating on its ground state wave function Ψ' should likewise be lower in energy than the expectation value of H' operating on any other wave function, including Ψ.

$$\mathrm{E}_0' = \langle\Psi'|\mathrm{H}'|\Psi'\rangle < \langle\Psi|\mathrm{H}'|\Psi\rangle \quad = \langle\Psi|\mathrm{H}'|\Psi\rangle + \langle\Psi|\mathrm{H}'-\mathrm{H}|\Psi\rangle \tag{2.3}$$
$$= \mathrm{E}_0 + \int \rho(\vec{\mathrm{r}})\,[\mathrm{v}'(\vec{\mathrm{r}}) - \mathrm{v}(\vec{\mathrm{r}})]\mathrm{d}\vec{\mathrm{r}}$$

Combining equations 2.2 and 2.3 to evaluate their coexistence leads to equation 2.4, which states the following contradiction.

$$\mathrm{E}_0 + \mathrm{E}_0' < \mathrm{E}_0' + \mathrm{E}_0 \tag{2.4}$$

Therefore we can conclude that given a particular $\rho(\vec{\mathrm{r}})$ there exists a unique $\mathrm{v}(\vec{\mathrm{r}})$. As such all other electronic properties can be determined.

The second Hohenberg-Kohn theorem then states, a trial density $\tilde{\rho}(\vec{\mathrm{r}})$, such that $\tilde{\rho}(\vec{\mathrm{r}}) \geq 0$, and $\int \tilde{\rho}(\vec{\mathrm{r}})\,\mathrm{d}\vec{\mathrm{r}} = \mathrm{N}$, will give an upper limit of the total energy. If we consider the ground state energy can be written,

$$\mathrm{E_v}(\rho) = \mathrm{T}(\rho) + \mathrm{V_{ne}}(\rho) + \mathrm{V_{ee}}(\rho) = \int \rho(\vec{\mathrm{r}})\mathrm{v}(\vec{\mathrm{r}})\mathrm{d}\vec{\mathrm{r}} + \mathrm{F_{HK}}[\rho] \tag{2.5}$$

where,

$$\mathrm{F_{HK}}[\rho] = \mathrm{T}(\rho) + \mathrm{V_{ee}}(\rho) \tag{2.6}$$

is the Hohenberg-Kohn universal functional. Then any trial density $\tilde{\rho}(\vec{r})$, according to the first theorem, would have its own potential $\mathrm{v}(\vec{r})$. This in turn causes it to have its own Hamiltonian H and wave function $\tilde{\Psi}$. Thus the expectation value would be,

$$\langle\tilde{\Psi}|\mathrm{H}|\tilde{\Psi}\rangle = \int \tilde{\rho}(\vec{r})\mathrm{v}(\vec{r})d\vec{r} + \mathrm{F_{HK}} = \mathrm{E_v}[\tilde{\rho}] \geq \mathrm{E_v}[\rho] \tag{2.7}$$

Now constraining the variation of total energy to the total number of electrons,

$$\delta\left\{\mathrm{E_v}[\rho] - \mu\left[\int \rho(\vec{r})d\vec{r} - \mathrm{N}\right]\right\} = 0 \tag{2.8}$$

leads us to the Euler-Lagrange equation,

$$\mu = \frac{\delta \mathrm{E_v}[\rho]}{\delta\rho(\vec{r})} = \mathrm{v}(\vec{r}) + \frac{\delta \mathrm{F_{HK}}}{\delta\rho(\vec{r})} \tag{2.9}$$

where the Lagrange multiplier μ is the chemical potential. Now if the exact form of the functional $\mathrm{F_{HK}}$ was known, the equation would then be exact for the ground state electron density.

The functional $\mathrm{F_{HK}}$ is defined only for those trial $\rho(\vec{r})$ that correspond to an anti-symmetric ground state wave function that is a solution to a particular Hamiltonian with external potentials $\mathrm{v}(\vec{r})$ (a.k.a. ν-representable). However the conditions for $\rho(\vec{r})$ to be ν-representable are unknown. Fortunately, DFT has the ability to be formulated on a density that can be derived from some arbitrary anti-symmetric wave function (N-representable).

The elimination of degeneracy limitations in the proof of the original Hohenberg-Kohn theorem was shown [28] with Levy's constrained search method using an N-

representable density as it is done in the following. Say a universal functional $F[\rho]$ is defined by the sums of kinetic $\left(T = \sum_i^N -\frac{1}{2}\nabla_i^2\right)$ and Coulomb repulsion energies $\left(V_{ee} = \sum_{i<j}^N \frac{1}{r_{ij}}\right)$,

$$F[\rho] = \min_{\Psi\to\rho}\langle\Psi|T + V_{ee}|\Psi\rangle \tag{2.10}$$

where all Ψ yield a fixed trial ρ that is N-representable. Now the ground state energy can be written as:

$$\begin{aligned} E_0 &= \min_{\Psi\to\rho}\left\langle\Psi\middle|T + V_{ee} + \textstyle\sum_i^N \nu(\vec{r})\ \middle|\Psi\right\rangle\} \\ &= \min_{\rho}\{\min_{\Psi\to\rho}\left\langle\Psi\middle|T + V_{ee} + \textstyle\sum_i^N \nu(\vec{r})\ \middle|\Psi\right\rangle\} \\ &= \min_{\rho}\{\min_{\Psi\to\rho}\langle\Psi|T + V_{ee}|\Psi\rangle\ +\ \int \nu(\vec{r})\rho(\vec{r})d\vec{r} \end{aligned} \tag{2.11}$$

Now using the definition of $F[\rho]$ from equation (2.10) we can write equation (2.11) as:

$$\begin{aligned} E_0 &= \min_{\rho}\left\{F[\rho] + \int \nu(\vec{r})\rho(\vec{r})d\vec{r}\right\} \\ &= \min_{\rho}\{E[\rho]\} \end{aligned} \tag{2.12}$$

where

$$E[\rho] = F[\rho] + \int \nu(\vec{r})\rho(\vec{r})d\vec{r} \tag{2.13}$$

In the constrained search formula for the functional $F[\rho]$ there is no reference to ρ needing to be ν-representable ground state density, as long as it is constructed from anti-symmetric wave functions. However, when ρ is ν-representable we get:

$$F[\rho] = F_{HK}[\rho] \tag{2.14}$$

The functional $F[\rho]$ is universal because it does not depend on the external potential $v(\vec{r})$. This constrained search method removes the degeneracy problem from the original Hohenberg-Kohn theorem, as only one set of the degenerate wave functions corresponding to ρ need be required.

2.3 The Kohn-Sham Method

The ground state electron density can be in principle determined by solving the Euler-Lagrange equation (2.9),

$$\mu = v(\vec{r}) + \frac{\delta F(\rho)}{\delta \rho(\vec{r})} \tag{2.15}$$

where μ is the Lagrange multiplier associated with the constraint $\int \rho(\vec{r})\, d\vec{r} = N$. The basic problem is to evaluate the kinetic energy term of the universal function (see equation (2.6)). Kohn-Sham proposed [29,30] an indirect approach to this problem.

Let us consider a non-interacting system where electrons move independently in a common local potential v_s, where the electronic density ρ is the same as the interacting electronic system. This can be done as long as we ensure that the wave functions, from which ρ is constructed are N-representable. In the Hamiltonian,

$$H_s = \sum_{i}^{N} \left(-\frac{1}{2}\nabla_i^2\right) + \sum_{i}^{N} v_s(\vec{r_i}) \tag{2.16}$$

there is no electron-electron repulsion term. For this system we can write the non-interacting wave function as the Slater determinant:

$$\Psi_s = \frac{1}{\sqrt{N!}} \det[\psi_1 \psi_2 \dots \psi_N] \tag{2.17}$$

where ψ_i are the N lowest eigenstates of the one-electron Hamiltonian h_s:

$$h_s\psi_i = \left[-\frac{1}{2}\nabla_i^2 + v_s(\vec{r_i})\right]\psi_i = \varepsilon_i\psi_i \tag{2.18}$$

The kinetic energy of this non-interacting system is,

$$T_s[\rho] = \left\langle \Psi_s \middle| \sum_{i=1}^{N}\left(-\frac{1}{2}\nabla_i^2\right) \middle| \Psi_s \right\rangle \tag{2.19}$$

$$= \sum_{i}^{N} \left\langle \psi_i \middle| \left(-\frac{1}{2}\nabla_i^2\right) \middle| \psi_i \right\rangle$$

while the density of the non-interacting system

$$\rho(\vec{r}) = \sum_{i}^{N} |\psi_i(\vec{x_i})|^2 \tag{2.20}$$

is equal to that of the interacting one.

As mentioned before the kinetic energy functional $T[\rho]$ is unknown, so we simply take the kinetic energy functional $T_s[\rho]$ of the non-interacting system instead of $T[\rho]$. Let the difference between these two functionals be $T_C = T - T_s$, and substituting this in equation (2.9) we get:

$$F[\rho] = T_s[\rho] + V_{ee}[\rho] + T_c[\rho] \tag{2.21}$$

The last two terms in the right hand side of equation (2.21) representing the electron-electron interaction and we can rewrite them as the Coulomb and exchange-correlation terms, respectively:

$$V_{ee}[\rho] + T_c[\rho] = J[\rho] + E_{XC}[\rho] \tag{2.22}$$

so equation (2.21) can be written as:

$$F[\rho] = T_s[\rho] + J[\rho] + E_{XC}[\rho] \tag{2.23}$$

Now with equation (2.23) the total energy shown in equation (2.13) can be written as:

$$\mathrm{E}[\rho] = \mathrm{T}[\rho] + \mathrm{J}[\rho] + \mathrm{E}_{\mathrm{XC}}[\rho] + \int \rho(\vec{r})v(\vec{r})d\vec{r} \tag{2.24}$$

Then the variation of equation (2.23) gives the Euler-Lagrange equation:

$$\begin{aligned} \mu = \frac{\delta \mathrm{E}[\rho]}{\delta\rho} &= \frac{\delta}{\delta\rho}\int \rho(\vec{r})v(\vec{r})d\vec{r} + \frac{\delta \mathrm{T}_s[\rho]}{\delta\rho} + \frac{\delta \mathrm{J}[\rho]}{\delta\rho} + \frac{\delta \mathrm{E}_{\mathrm{XC}}[\rho]}{\delta\rho} \\ &= v(\vec{r}) + \frac{\delta \mathrm{T}_s[\rho]}{\delta\rho} + \frac{\delta \mathrm{J}[\rho]}{\delta\rho} + \frac{\delta \mathrm{E}_{\mathrm{XC}}[\rho]}{\delta\rho} \\ &= v_{\mathrm{eff}}(\vec{r}) + \frac{\delta \mathrm{T}_s[\rho]}{\delta\rho} \end{aligned} \tag{2.25}$$

where the Kohn-Sham effective potential is defined by:

$$\begin{aligned} v_{\mathrm{eff}}(\vec{r}) &= v(\vec{r}) + \frac{\delta \mathrm{J}[\rho]}{\delta\rho} + \frac{\delta \mathrm{E}_{\mathrm{XC}}[\rho]}{\delta\rho} \\ &= v(\vec{r}) + \int \frac{\rho(\vec{r}')}{|\vec{r} - \vec{r}'|}d\vec{r}' + v_{\mathrm{XC}}(\vec{r}) \end{aligned} \tag{2.26}$$

defining the exchange-correlation potential as:

$$v_{\mathrm{XC}}(\vec{r}) = \frac{\delta \mathrm{E}_{\mathrm{XC}}[\rho]}{\delta\rho} \tag{2.27}$$

Now rewriting equation (2.24) in terms of one electron orbitals:

$$\mathrm{E}(\rho) = \sum_{i}^{N} \int \psi_i^* \left(-\frac{1}{2}\nabla^2\right)\psi_i d\vec{r} + \mathrm{J}[\rho] + \mathrm{E}_{\mathrm{XC}}[\rho] + \int \rho(\vec{r})v(\vec{r})d\vec{r} \tag{2.28}$$

and the electron density is given in equation (2.20). Thus the energy is expressed in terms of N orbitals. Taking the variation of this energy with respect to the one-electron orbital ψ_i, along with the constraint that they be orthonormal to each other:

$$\int \psi_i^* \psi_j d\vec{x} = \delta_{ij} \tag{2.29}$$

we get,

$$\delta \left[E[\rho] - \sum_i^N \sum_j^N \varepsilon_{ij} \int \psi_i^*(\vec{x}) \psi_j(\vec{x}) d\vec{x} \right] = 0 \tag{2.30}$$

In equation (2.37) ε_{ij} are the Lagrange multipliers. Now considering the variation of equation (2.28) we get:

$$\delta E[\rho] = \left[\frac{\delta}{\delta \psi_i^*} \sum_i^N \int \psi_i^* \left(-\frac{1}{2} \nabla^2 \right) \psi_i d\vec{r} + \frac{\delta J}{\delta \psi_i^*} + \frac{\delta E_{XC}}{\delta \psi_i^*} + \frac{\delta}{\delta \psi_i^*} \int v\,(\vec{r}) \left(\sum_i^N |\psi_i|^2 \right) d\vec{r} \right] \delta \psi_i^* \tag{2.31}$$

Using the chain rule for the functional derivative, the first term on the right hand side gives,

$$\frac{\delta}{\delta \psi_i^*} \sum_i^N \int \psi_i^* \left(-\frac{1}{2} \nabla^2 \right) \psi_i d\vec{r} = \frac{\partial \psi_i^*}{\partial \psi_i^*} \left(-\frac{1}{2} \nabla^2 \right) \psi_i + \psi_i^* \frac{\partial}{\partial \psi_i^*} \left\{ -\frac{1}{2} \nabla^2 \right\} \tag{2.32}$$

$$= -\frac{1}{2} \nabla^2 \psi_i$$

where the derivative in the second term is zero. Similarly the last term in the variation of energy in equation (2.31) gives,

$$\frac{\delta}{\delta\psi_i^*}\int v(\vec{r})\left(\sum_i^N|\psi_i|^2\right)d\vec{r} = v(\vec{r})\psi_i \tag{2.33}$$

So from equation (2.30), for any arbitrary variation of $\delta\psi_i^*$, we get using equations (2.32) and (2.33),

$$h_{eff}\psi_i = \left[-\frac{1}{2}\nabla^2 + \frac{\delta J[\rho]}{\delta\rho} + \frac{\delta E_{XC}}{\delta\rho} + v(\vec{r})\right]\psi_i = \sum_j^N \varepsilon_{ij}\psi_j \tag{2.34}$$

$$\Rightarrow h_{eff}\psi_i = \left[-\frac{1}{2}\nabla^2 + v_{eff}(\vec{r})\right]\psi_i = \sum_j^N \varepsilon_{ij}\psi_j$$

where $v_{eff}(\vec{r})$ is defined by equation (2.26). Now in equation (2.34) the Hamiltonian h_{eff} is a Hermitian operator, hence ε_{ij} is a Hermitian matrix which can be diagonalized by unitary transformation, leading to the Kohn-Sham equations:

$$\left[-\frac{1}{2}\nabla^2 + v_{eff}(\vec{r})\right]\psi_i = \varepsilon_i\psi_i \tag{2.35}$$

Equation (2.35) (or equation (2.41)) is the central equation in the application of density functional theory. These equations are usually solved by self-consistent methods which can be represented by the following flow chart:

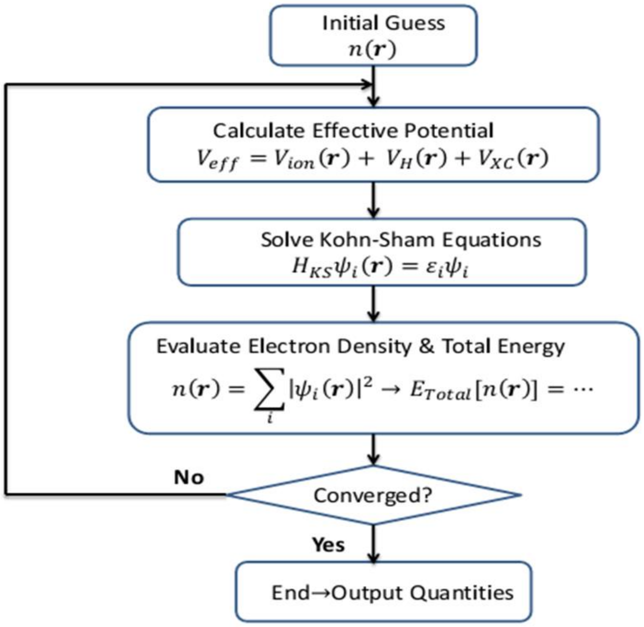

Figure 2.1 A schematic representation of the self-consistent cycle as it is implemented in DFT algorithms.

The solution of the Kohn-Sham equation is in principle exact, but as can be seen from the above discussion of the Kohn-Sham procedure that, it does not give any prescription of obtaining the exchange-correlation functionals. Depending on the system at hand, different levels of approximations were made to deal with this functional. In the following we will describe the local and generalized density approximations to these functionals.

2.4 Local Density Approximations: LDA

Historically local density approximation to the functionals is the most used approach in the condensed matter physics. In this approximation the functionals are local, that is they depend on the local variable. Formally, a functional F is local if,

$$\mathrm{F}[\rho] = \int \mathrm{f}(\rho(\vec{\mathrm{r}}))\mathrm{d}\vec{\mathrm{r}} \tag{2.36}$$

where the functional F depends on $\vec{\mathrm{r}}$ only through the density $\rho(\vec{\mathrm{r}})$. Physically this approximation would be correct in the limit where the charge density is a slowly varying function with respect to the spatial variable, $\vec{\mathrm{r}}$. Within LDA the exchange and correlation energy becomes,

$$\mathrm{E}_{\mathrm{XC}}^{\mathrm{LDA}}[\rho] = \int \rho(\vec{\mathrm{r}})\varepsilon_{\mathrm{XC}}(\rho)\mathrm{d}\vec{\mathrm{r}} \tag{2.37}$$

where $\varepsilon_{\mathrm{XC}}(\rho)$ is the exchange and correlation energy per particle of a uniform electron gas of density $\rho(\vec{\mathrm{r}})$. The exchange and correlation potential then is given by,

$$\mathrm{v}_{\mathrm{XC}}^{\mathrm{LDA}}(\vec{\mathrm{r}}) = \frac{\delta \mathrm{E}_{\mathrm{XC}}^{\mathrm{LDA}}}{\delta\rho(\vec{\mathrm{r}})} = \varepsilon_{\mathrm{XC}}\big(\rho(\vec{\mathrm{r}})\big) + \rho(\vec{\mathrm{r}})\frac{\partial\varepsilon_{\mathrm{XC}}}{\partial\rho} \tag{2.38}$$

Then the Kohn-Sham equation can be written as,

$$\left[-\frac{1}{2}\nabla^2 + \mathrm{v}(\vec{\mathrm{r}}) + \int \frac{\rho(\vec{\mathrm{r}}')}{|\vec{\mathrm{r}} - \vec{\mathrm{r}}'|}\mathrm{d}\vec{\mathrm{r}}' + \mathrm{v}_{\mathrm{XC}}^{\mathrm{LDA}}(\vec{\mathrm{r}})\right]\psi_{\mathrm{i}} = \varepsilon_{\mathrm{i}}\psi_{\mathrm{i}} \tag{2.39}$$

Now the function $\varepsilon_{\mathrm{XC}}(\rho)$ can be divided into exchange and correlation contributions [31],

$$\varepsilon_{\mathrm{XC}}(\rho) = \varepsilon_{\mathrm{X}}(\rho) + \varepsilon_{\mathrm{C}}(\rho) \tag{2.40}$$

where $\varepsilon_{\mathrm{X}}(\rho)$ is the Dirac exchange energy,

$$\varepsilon_{\mathrm{XC}}(\rho) = -\frac{3}{4}\left(\frac{3}{\pi}\right)^{1/3} \rho(\vec{\mathrm{r}})^{1/3} \tag{2.41}$$

and $\varepsilon_{\mathrm{C}}(\rho)$ is the correlation energy per particle of a homogeneous electron gas,

$$\varepsilon_{\mathrm{C}}(\rho) = \begin{cases} 0.0311\ln \mathrm{r_s} - 0.048 + \mathrm{r_s}(\mathrm{A}\ln \mathrm{r_s} + \mathrm{C}) & \text{for } \mathrm{r_s} \ll 1 \\ \dfrac{1}{2}\left(\dfrac{\mathrm{g_0}}{\mathrm{r_s}} + \dfrac{\mathrm{g_1}}{\mathrm{r_s^{3/2}}} + \dfrac{\mathrm{g_2}}{\mathrm{r_s^2}} + \cdots\right) & \text{for } \mathrm{r_s} \gg 1 \end{cases} \tag{2.42}$$

where, $\mathrm{r_s}$ is the Wigner-Seitz radius,

$$\frac{4}{3}\pi r_s^3 = \frac{1}{n} \tag{2.43}$$

We can extend LDA to include spin for so-called unrestricted calculations. We can divide the total electronic density in two parts for spin up density (ρ_α) and spin down (ρ_β), so that,

$$\rho_\alpha(\vec{r}) + \rho_\beta(\vec{r}) = \rho(\vec{r}) \tag{2.44}$$

Then in the local spin density approximation the exchange-correlation functional can be written as,

$$E_{XC}^{LSD}[\rho_\alpha, \rho_\beta] = \int \rho(\vec{r})\varepsilon_{XC}\left(\rho_\alpha(\vec{r}), \rho_\beta(\vec{r})\right) d\vec{r} \tag{2.45}$$

As mentioned earlier, LDA (or LSD) is based upon the idealization that the system is a homogeneous electron gas with equal (or slowly varying) density. It is obvious that any real system could behave in a drastically manner. However, the success and importance of the local density approximation in condensed matter physics is noteworthy. It gives results comparable or better than Hartree-Fock approximation.

2.5 Generalized Gradient Approximation

Logically the first step to improve upon the LDA is to take into account the spatial change in electronic density, i.e. the gradient of the density, $\nabla\rho(\vec{r})$, to take into account the non-homogeneity of the true electron density. This method is named as the gradient expansion approximation (GEA). This can be done by a Taylor series expansion of the exchange-correlation functional,

$$E_{XC}^{GEA}[\rho_\alpha, \rho_\beta] = \int \rho(\vec{r})\varepsilon_{XC}\left(\rho_\alpha(\vec{r}), \rho_\beta(\vec{r})\right) d\vec{r} + \sum_{\sigma,\sigma'} \int C_{XC}^{\sigma,\sigma'}(\rho_\alpha, \rho_\beta) \frac{\nabla\rho_\alpha}{\rho_\sigma^{2/3}} \frac{\nabla\rho_\beta}{\rho_\sigma^{2/3}} d\vec{r} + \cdots \tag{2.46}$$

The coefficient $C_{XC}^{\sigma,\sigma'}$ in equation (2.46) was found to be proportional to $1/\rho^{4/3}$. Unfortunately, GEA did not give a systematic improvement on the LDA approximation. The reason that the exchange-correlation interation was not physically very meaningful in this definition. In addition to it, higher order corrections of $\nabla\rho's$ are exceedingly difficult to calculate. However, a more sophisticated approach to include the gradient of densities was proposed by Perdew and others [25,32–34] called generalized gradient approximation (GGA), which defines the exchange-correlation functional in the following manner,

$$E_{XC}^{GGA}[\rho_\alpha, \rho_\beta] = \int f(\rho_\alpha, \rho_\beta, \nabla\rho_\alpha, \nabla\rho_\beta)\, d\vec{r} \tag{2.47}$$

In practice, E_{XC}^{GGA} is divided into its exchange and correlation contributions,

$$E_{XC}^{GGA} = E_X^{GGA} + E_C^{GGA} \tag{2.48}$$

and the approximations for the functionals are usually made individually.

It should be mentioned here that GGA does not provide a complete non-local functional. In true mathematical sense, $\rho(\vec{r})$, and its gradient $\nabla\rho(\vec{r})$ depend only on $\vec{r}$, and is independent of any $\rho(\vec{r}')$, where $\vec{r}' \neq \vec{r}$. Only advantage GGA achieved is that it includes the local variation of the densities. Also GGA in its original form does not produce the simultaneous asymptotic behavior for both the energy and the potentials. In the modern day functionals, a cut-off procedure on density is used to produce the satisfactory results. However GGA functionals so show improvements over LDA functionals in many systems in condensed matter physics and quantum chemistry, with the exception in the long range weakly bound system, for instance in van der Waals interaction.

2.6 DFT +U

The DFT+U method employs a Hartree-Fock treatment of the on-site interactions, which are characterized as interactions between electrons of the same angular momentum l that are localized in atomic-like orbitals on the same atom I, and uses DFT methods to describe all other interactions in the system. This is achieved with the following general functional form:

$$\mathrm{E^{DFT+U}[\rho, \{n_{Ilm\sigma}\}] = E^{DFT}[\rho] + E^{on-site}[\{n_{Ilm\sigma}\}] - E^{dc}[\{N_{Il\sigma}\}]} \qquad (2.49)$$

where $\mathrm{E^{DFT}}$ is the DFT energy of the system based on the total electron density ρ, $\mathrm{E^{on-site}}$ is the on-site energy, and $\mathrm{E^{dc}}$ is a double-counting term that corrects for the fact that the on-site interactions are included in both $\mathrm{E^{DFT}}$ and $\mathrm{E^{on-site}}$. $\mathrm{n_{Ilm\sigma}}$ corresponds to the number of electrons with spin σ, angular momentum l, and magnetic quantum number m that are localized on atom I. In practice, the values of $\mathrm{n_{Ilm\sigma}}$ are obtained by projecting Kohn-Sham orbitals for the entire system onto a suitable set of atom-centered basis functions. The quantity $\mathrm{N_{Il\sigma}}$ is the number if electrons of angular momentum l and spin σ that are localized on atom α and is given by $\mathrm{N_{Il\sigma} = \sum_m n_{Ilm\sigma}}$.

Here, we will focus on the DFT+U formalism developed by Dudarev et al [35]., which is implemented in the VASP electronic structure package. In this formalism, $\mathrm{E^{on-site}}$ and $\mathrm{E^{dc}}$ are defined as:

$$E^{\mathrm{on-site}}[\{n_{Ilm\sigma}\}] = \left(\sum_{m,m'} n_{Ilm\alpha} n_{Ilm'\beta} + \sum_{m,m'>m} n_{Ilm\alpha} n_{Ilm'\alpha} + \sum_{m,m'>m} n_{Ilm\beta} n_{Ilm'\beta}\right) U_{Il} - \left(\sum_{m,m'>m} n_{Ilm\alpha} n_{Ilm'\alpha} + \sum_{m,m'>m} n_{Ilm\beta} n_{Ilm'\beta}\right) J_{Il} \tag{2.50}$$

$$E^{\mathrm{dc}}[\{N_{Il\sigma}\}] = \left(N_{Il\alpha} N_{Il\beta} + \frac{N_{Il\alpha}(N_{Il\alpha} - 1)}{2} + \frac{N_{Il\beta}(N_{Il\beta} - 1)}{2}\right) U_{Il} - \left(\frac{N_{Il\alpha}(N_{Il\alpha} - 1)}{2} + \frac{N_{Il\beta}(N_{Il\beta} - 1)}{2}\right) J_{Il} \tag{2.51}$$

Note that for the sake of clarity, these definitions have been written to describe the on-site and double-counting energies arising from electrons of a particular angular momentum on a single atom. In a polyatomic system, there would be a summation over multiple atoms and different values of l in accordance with the nature of the localized electrons in the system.

The quantities U_{Il} and J_{Il} in equations (2.50) and (2.51) correspond to the spherically-averaged Coulomb and exchange interactions between electrons of angular momentum l that are localized on the same atom I. Using these quantities, equation (2.50) provides a HF-like treatment of the on-site interaction energies, assuming that the Coulomb and exchange interactions are independent of m. The expression for E^{dc} is approximate and essentially enumerates the on-site interactions that are accounted for in E^{DFT}. Justifications for this particular form of E^{dc} have been made elsewhere, and will not be discussed here.

Inserting the definitions of $\mathrm{E}^{\text{on-site}}$ and E^{dc} in equations (2.50) and (2.51) into equation (2.49) leads to the following expression for $\mathrm{E}^{\mathrm{DFT+U}}$:

$$\mathrm{E}^{\mathrm{DFT+U}}[\rho, \{\mathrm{n}_{\mathrm{Ilm}\sigma}\}] = \mathrm{E}^{\mathrm{DFT}}[\rho] + \sum_{\mathrm{I,l,m},\sigma} \frac{(\mathrm{U}_{\mathrm{Il}} - \mathrm{J}_{\mathrm{Il}})}{2} (\mathrm{n}_{\mathrm{Ilm}\sigma} - \mathrm{n}_{\mathrm{Ilm}\sigma}^{2}) \tag{2.52}$$

where the summation in the second term on the right hand side has been written in a general sense for a polyatomic system. In practice, this summation would include values of I and l that are consistent with the localized electrons of the system. Unfortunately, this expression in not invariant with respct to unitary transformations of orbitals. To achieve rotational invariance, the occupation numbers in equation (2.52) must be replace by the on-site density matrix of the localized electrons, $\rho_{\mathrm{jk}}^{\mathrm{Il}\sigma}$. Doing this leads to the following DFT+U total energy functional:

$$\mathrm{E}^{\mathrm{DFT+U}}[\rho] = \mathrm{E}^{\mathrm{DFT}}[\rho] + \sum_{\mathrm{I,l},\sigma,\mathrm{j,k}} \frac{(\mathrm{U}_{\mathrm{Il}} - \mathrm{J}_{\mathrm{Il}})}{2} \left[\rho_{\mathrm{jj}}^{\mathrm{Il}\sigma} - \rho_{\mathrm{jk}}^{\mathrm{Il}\sigma}\rho_{\mathrm{kj}}^{\mathrm{Il}\sigma}\right] \tag{2.53}$$

Note equations (2.52) and (2.53) are equivalent when the on-site density matrix is diagonal.

The first term on the right hand side of equation (2.53) corresponds to the DFT energy based on the total electron density of the system and the second term can be interpreted as a penalty function that modulates the electron density associated with the localized states. Noting that $\mathrm{U}_{\mathrm{Il}} > \mathrm{J}_{\mathrm{Il}}$ and $\sum_{\mathrm{jk}}\left[\rho_{\mathrm{jj}}^{\mathrm{Il}\sigma} - \rho_{\mathrm{jk}}^{\mathrm{Il}\sigma}\rho_{\mathrm{kj}}^{\mathrm{Il}\sigma}\right] > 0$, it becomes evident that this is a positive definite penalty function driving the on-site density matrix toward idempotency. This property of the penalty function biases the localized states toward integer occupations, which counters the tendency of DFT calculations to fractionally occupy these states (as in a metal).

The one-electron potential, $V_{jk}^{Il\sigma}$, of the localized orbitals can be obtained by differentiating E^{DFT+U} with respect to $\rho_{jk}^{Il\sigma}$:

$$V_{jk}^{Il\sigma} = \frac{\delta E^{DFT}}{\delta \rho_{jk}^{Il\sigma}} + (U_{Il} - J_{Il})\left(\frac{1}{2}\delta_{jk} - \rho_{jk}^{Il\sigma}\right) \tag{2.54}$$

In the limit of integer occupations of the localized states, this has the effect of shifting the energies of the occupied localized orbitals by $(U_{Il} - J_{Il})/2$, increasing the band gap by $U_{Il} - J_{Il}$. This property counteracts the tendency of DFT calculations to greatly underestimate the band gaps of strongly correlated electron materials.

Chapter 3

Material Analysis

3.1 Introduction

The most rigorous material analyses and characterization methods of oxide photocatalysts typically consists of the latest spectroscopic and microscopic techniques. Scanning electron microscopy (SEM), high resolution transmission electron microscopy (HRTEM), electron dispersive spectroscopy (EDS), x-ray photoelectron spectroscopy (XPS) and x-ray diffraction (XRD) are among these advance characterization methods. Physical features of photocatalysts powders can be extrapolated from raster images created by SEM, while chemical composition and crystalline features can be extrapolated from those created by EDS and XRD, respectively. More advanced material analyses are done with XPS and HRTEM which require intuitive manipulations of the data to determine ion charges and stoichiometry. However, the readiness to couple these analyses can lead to erroneous results and misconceptions.

In particular workers generally rely on XRD and XPS to confirm whether or not an impurity takes up a particular substitutional site. Take for example XRD results that indicate a particular a cubic crystalline structure, which HRTEM and EDS analyses suggest are aggregates made of multiples of two Bi cations, two Ti cations and seven O anions. Thereby subsequent XPS analysis is inadvertently biased toward a particular ionic state of the elemental constituents (Bi^{3+}, Ti^{4+}, and O^{2-}) in order to coincide with this data. Given the resolution levels of XPS and XRD are vastly different and multi metal oxides incur anion deficiencies due to a charge compensation mechanism, makes answering questions like: Would a transition metal with a charge state of 3+ substitute Ti cations or Bi cations? or, does this transition metal have octahedral or tetrahedral coordination with O anions?, exercises in educated guessing.

We suggest theory that examines the possible outcomes in a probabilistic manner to be superior to educated guesses. We attempt to ultimately demonstrate the advantages of coupling theoretical methods with experimental ones for the development of higher quality modified mixed metal oxide photocatalysts. In this chapter we introduce our theoretical method for developing free energy landscape (FEL) phase diagrams for doped multi metal oxide photocatalysts. As doping is a band engineering technique that can overcome the limitations of optical absorption, there is a need to examine practical approaches to enhancing stability of these materials once it is done. We have seen from a previous experimental study [36] that a critical dopant concentration (threshold) marks the limit of how much a multi metal oxide photocatalyst can be enhanced before dopant inspired phases (DIPs) or secondary phases occur. Therefore we take suppression of DIPs and secondary phase formations to be a crucial first step associated with enhancing the photocatalytic properties. Evidently, distinct thermodynamic relationships can be defined and explored theoretically that shed light on how pure phase doping in experiment can be obtained.

3.2 Computational Details of the Free Energy Landscape

Our DFT calculations for the stability analysis purpose were performed using the Vienna Ab Initio Simulation Package (VASP) [37–39]. VASP uses the projector augmented wave (PAW) method with crystal wave functions expanded in terms of a plane wave basis set to describe interactions between core and valence electrons. The PBE (Perdew-Burke-Ernzerhof) exchange-correlation functional was used as it is still the best known functional for general accuracy and applicability at the DFT level [25]. The starting atomic coordinates were defined by the respective material unit cell. Full relaxation was based on the residual forces between atoms becoming lower than 0.01 eV/Å. The Brillouin zones were sampled with a saturated grid densities, 6 X 6 X 8 for rutile TiO_2, 4 X 4 X 6 for clinobisvanite $BiVO_4$, and 5 X 5 X 5 for pyrochlore $Bi_2Ti_2O_7$. In recognition of the adequacy of our computational details, the obtained lattice parameters for pristine BTO were a = b = c = 10.329 Å and α = β = γ = 90° which agrees well with other theoretical [40–42] and experimental [43–45] results.

After the total energies and electronic structures were obtained for all phases and defect containing structures, we determined their formation enthalpies and defect formation energies. Formation enthalpy (equation (3.1)) of any DFT calculated structure can be defined as the energy difference between its total energy E_t and the combination of atomic energies (chemical potentials, μ_i) required to compose the structure; here n_i is the total number of i^{th} atoms.

$$\Delta H_f = E_t - \sum_i n_i \mu_i \tag{3.1}$$

The doping formation energy can be defined as the sum of two differences (equation (3.2)). The first difference is of the total energy between the unit cell with doped and the pristine unit cell, e.g. the energy gained or loss by forming the defect. The second difference is written in summation form where each term has an operator α associated with it. This operator becomes either a negative sign or a positive sign depending on i^{th} atoms added or removed to form the cell.

$$E_f(\mu) = E_d - E_t + \sum_i \alpha_i n_i \mu_i \tag{3.2}$$

For a deeper analytical purpose we consider the variation in atomic chemical potentials due to the atomic source. Hence μ_i represents the atomic energy plus some additional free energy due to where the atom came from (see equation (3.3)). When used with equation (3.1), a constrained linear equation can be generated that allows us to evaluate formation of Fe-BTO given different combinations of additional free energy.

$$\mu_i = \mu_i^0 + \Delta\mu_i \tag{3.3}$$

This scope dictates thermodynamic limits be imposed on the additional free energy. For instance, to avoid solutions to the constrained equation that would result in atomic dissociation we impose an upper bound on $\Delta\mu_i$. Consequently, this assures $\Delta\mu_i$ is always an energy gain.

$$\Delta\mu_i \leq 0 \text{ eV} \tag{3.4}$$

This upper bound on the free energy is referred to throughout the remaining text as the rich condition. Therefore given a rich supply of any elemental constituent its $\Delta\mu_i$ term is at most equal to zero. The rich condition serves as a universal reference point for all constituents and phases, values greater than zero imply an input of energy from an external source.

3.3 Clinobisvanite $BiVO_4$ (BVO)

3.3.1 Structural Properties of BVO

$BiVO_4$ has attracted attention due to its high photocatalytic activity for oxygen evolution in aqueous solutions under visible light irradiation relative to other known materials tested under similar conditions and has earned recognition as the most efficient hydrogen producing oxide photocatalyst. $BiVO_4$ exists in three main polymorphs: the zircon structure with tetragonal crystal system and the scheelite structure with monoclinic and tetragonal crystal systems. The scheelite structure with monoclinic crystal system, also known as clinobisvanite (BVO), has been reported as the most photoactive form of $BiVO_4$ and is shown in figure 3.1.

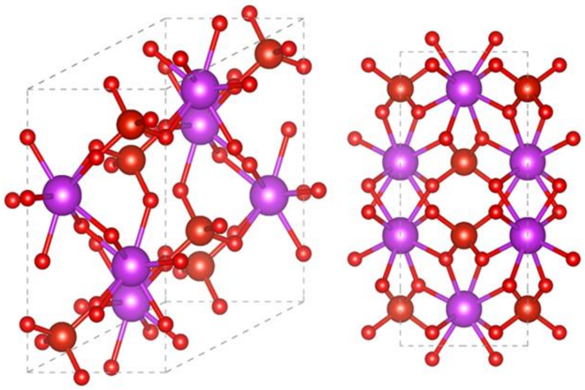

Figure 3.1 Clinobisvanite (BVO) crystal structure. Bi atoms are represented by the large purple spheres, V atoms are represented by the middle-sized burgundy spheres, and O atoms are represented by the small red spheres. Structural images were generated using the Visualization for Electronic and Structural Analysis program (VESTA) [46].

A mixed cation coordination of BVO can be seen in figure 3.1. Bi atoms are coordinated with eight O atoms while V atoms are coordinated with four O atoms. This aspect of the structure is an important observation when determining impurity substitutions intended for a particular cation. For instance, W and Mo are two common dopants in BVO that both improve spectral absorption, but due to the effect on photogenerated charge carriers, the photoactivity is quite different. W and Mo are both n-type dopants in BVO based on their 6+ oxidation state. Yet the evidence put forth by the literature indicates W is the better dopant. In a comprehensive study on the factors associated with metal doping BVO for improved photocatalytic performance [47] the authors conclude W and Mo are both revealed as excellent shallow dopants, which facilitate the separation of excited electron-hole pairs, but due to their difference in ionization energy W can more efficiently donate electrons to the host lattice than Mo. In both cases subsequent doping leads to a shift in the symmetry from monoclinic to tetragonal which reportedly have significant differences in photoactivity between the two symmetries. We suggest this difference in ionization ultimately effects the cation site that is more readily substituted. Take for example the case where either of these dopants actually replace a Bi atom instead of a V atom. In reference 33 the authors discuss a merging of XRD peaks representing (200) and (002) lattice planes at different doping concentrations which could only be attributed to a mechanism that promotes secondary phase formations.

3.3.2 Electronic Properties of BVO

In figure 3.2 we show our GGA-DFT calculated electronic structure of monoclinic $BiVO_4$. It shows the electronic band structure and density of states projected on select atomic orbitals for Bi, V, and O ions. The Bi-O interaction leads to the hybridization between Bi 6s and O 2p where the antibonding state makes up the valence band maximum (VBM). The bonding state (not shown) is around 9-10 eV below the Fermi energy level.

The band gap of monoclinic $BiVO_4$ is reported to be 2.3-2.4 eV by experiment and is shown to be an indirect band gap around 2.05 eV as indicated from our DFT calculations. Based on the stoichiometry of $BiVO_4$, the oxidation states and atomic orbitals are given by Bi^{3+} ($5d^{10}6s^2$), V^{5+} ($3d^0$), and O^{2-} ($2p^6$). The VB and CB mainly consist of O 2p states and V 3d states. The Bi 6p and 6s states also contribute to the composition of VB and CB. Because of the V tetrahedron ligand field the V 3d states are split into e and t_2 states features which are consistent with previous calculations. From the curvature of the band edges, the effective hole and electron masses are roughly estimated to be $0.42m_e$ and $0.60m_e$.

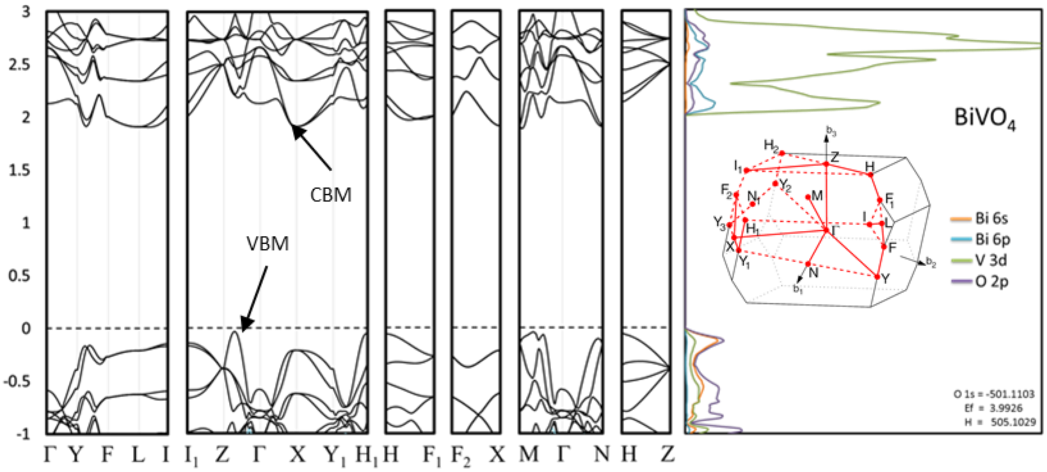

Figure 3.2 BVO electronic band structure and density of states projected on the Bi 6s (orange), Bi 6p (cyan), V 3d (green), and O 2p (purple) states. The horizontal dotted line indicates the Fermi energy level, which is set to 0 eV. The inset is of the Brillouin zone of monoclinic BVO with reciprocal lattice vectors (b_1, b_2, and b_3) and the $MCLC_5$ path indicated.

In terms of photocatalytic performance, the conduction band edge of $BiVO_4$ has been estimated to be at 0 V vs. NHE at pH 0, which corresponds to a valence band edge of 2.4 V vs. NHE at pH 0 (using 2.4 eV as the band gap). Since the conduction band is not more negative than the H^+ reduction potential (0.0 V vs. NHE at pH 0), pure $BiVO_4$ cannot evolve substantial amounts of H_2 from H_2O without an applied bias on an inert metal counter-electrode. On the other hand, the valence band of $BiVO_4$ is below the water oxidation potential (1.23 V vs. NHE at pH 0) indicting that $BiVO_4$ is thermodynamically capable of evolving O_2 from H_2O. Several researchers have confirmed that $BiVO_4$ can oxidize water by measuring O_2 evolution from aqueous solutions containing Ag^+ as a sacrificial reagent (Ag^+/Ag redox potential at 0.799 V vs. NHE). Although $BiVO_4$ is not able to reduce H^+, with a counter-electrode and bias it is still a promising material for the overall water splitting reaction as a photoanode in a multi-photon PEC cell.

3.3.4 Electronic Structure of Metal Doped BVO

We examined antimony and tantalum as dopants in BVO to determine the relative effects on its band edges and charge carrier properties. In figure 3.3 and 3.4 we show our calculated electronic structure of the Ta and Sb substitutional doping, respectively. According to the electronic configurations of Ta and Sb and also the defect formation energies of each doping we find Ta in V sites (Ta_V) and Sb in Bi sites (Sb_{Bi}) to be the most stable doping configurations in comparison to their respective counterparts Ta_{Bi} an Sb_V.

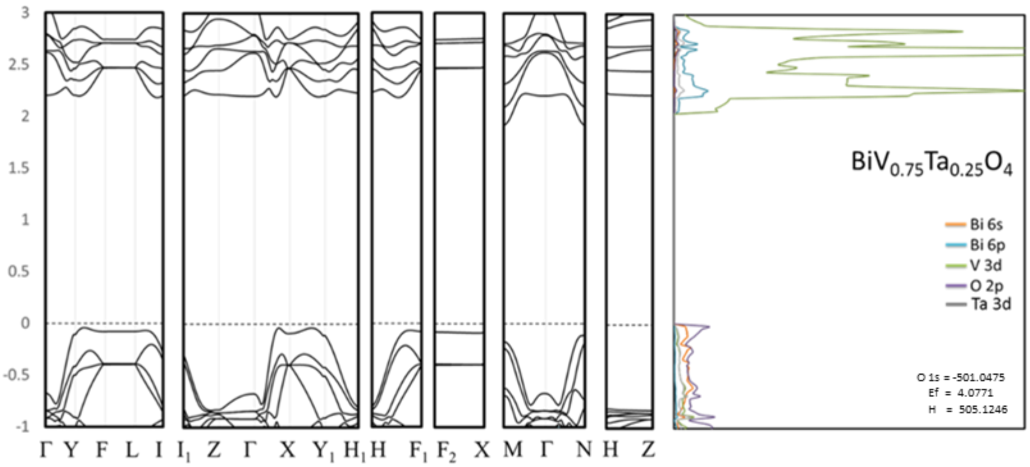

Figure 3.3 Electronic band structure and density of states projected on Bi 6s (orange) Bi 6p (cyan), V 3d (green), O 2p purple and Ta 3d (grey) atomic orbitals. V is substituted by Ta (Ta_V) according to the shown concentration. The horizontal line represents the Fermi energy level which is set to 0 eV.

In the case of Ta_V the GGA-DFT calculated band gap is ~ 2 eV as it was in the pristine BVO case. Likewise, the Fermi energy level, measured from the core O 1s levels, indicates the band edges are also unchanged. Furthermore the overall chemical composition of the bands is virtually unchanged, except for the presence of Ta 3d in the VB and CB. The interesting effect is related to the dispersion of the electronic bands. Due to the lack of dispersion, Ta doping apparently increases the effective masses and reduces the mobility of charges. Thus incorporation of Ta 3d states negatively affects the collective properties associated with enhancing photocatalytic performance.

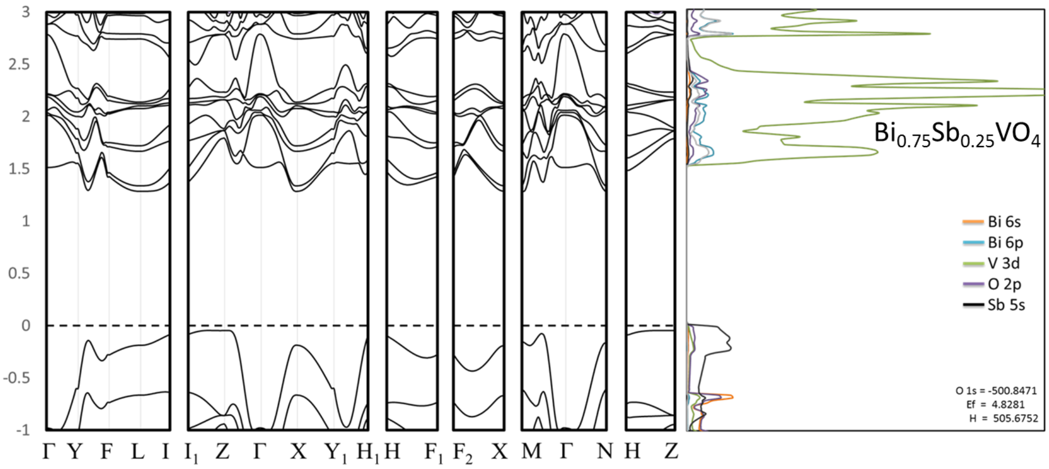

Figure 3.4 Electronic band structure and density of states projected on Bi 6s (orange) Bi 6p (cyan), V 3d (green), O 2p purple and Sb 5s (black) atomic orbitals. Bi is substituted by Sb (Sb_{Bi}) according to the shown concentration. The horizontal line indicates the Fermi energy level which is set to 0 eV.

For the case of Sb_{Bi} doping, it can be seen in figure 3.4 that the band gap is reduced considerably by introducing the Sb 5s electronic states. The valence band maximum is approximately 0.7 eV closer to the conduction band than it previously was without Sb doping. According to the differences between the O 1s levels of the electronic core between pristine BVO and Sb_{Bi}, the valence band edge was raised. From the projected density of states, shown in figure 3.4, it can be seen that the Sb 5s level sits atop the Bi 6s level to form the VBM which accounts for the increased VBM height.

Among the two dopant considered here, Sb is the most advantageous for improving the water oxidation reaction.

This type of electronic structure analysis demonstrates the relative ease associated with selecting impurities based on their potential for improving photocatalytic performance. Yet these potential electronic enhancements do not reflect the effective conditions necessary to achieve similar results in experiment. To determine such conditions we rely on our method for stability analysis described in section 3.2. Therefore, in the following section we describe our theoretical method in detail with respect to the Sb_{Bi} doping configuration.

3.3.5 Free Energy Landscape Analysis of Sb-BVO

To begin our free energy landscape (FEL) analysis we first calculated the total energies and formation enthalpies of the binary analogues of BVO and some of the probable DIPs which are shown in table 3.1. The quantity that is shown in green represents the highest lower limit of available O free energy that will ensure all phases can be formed within the FEL.

Table 3.1 Total energies, binding energies (BE), formation energies and the respective O free energy limit all in eV of Sb-doped BVO, BVO's binary analogues and some DIPs.

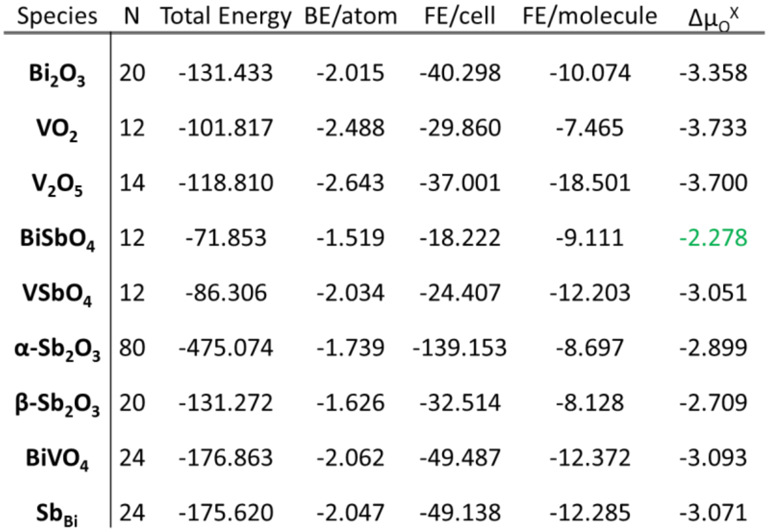

Species	N	Total Energy	BE/atom	FE/cell	FE/molecule	$\Delta\mu_O{}^X$
Bi_2O_3	20	-131.433	-2.015	-40.298	-10.074	-3.358
VO_2	12	-101.817	-2.488	-29.860	-7.465	-3.733
V_2O_5	14	-118.810	-2.643	-37.001	-18.501	-3.700
$BiSbO_4$	12	-71.853	-1.519	-18.222	-9.111	-2.278
$VSbO_4$	12	-86.306	-2.034	-24.407	-12.203	-3.051
α-Sb_2O_3	80	-475.074	-1.739	-139.153	-8.697	-2.899
β-Sb_2O_3	20	-131.272	-1.626	-32.514	-8.128	-2.709
$BiVO_4$	24	-176.863	-2.062	-49.487	-12.372	-3.093
Sb_{Bi}	24	-175.620	-2.047	-49.138	-12.285	-3.071

The values shown in table 3.1 define several constraints for the constituent elements.

$$n_i\Delta\mu_i < \Delta H_f^X = \text{FE/molecule} \tag{3.5}$$

Equation 3.5 is a general form of the constraints when equations 3.1 and 3.3 are combined. X represents one of the listed chemical species and FE/molecule refers to the corresponding value given in table 3.1. The quantities are then plugged into the specific equation for the formation enthalpy of the Sb_{Bi} doping configuration given in equation 3.6.

$$\Delta H_f^{Sb_{Bi}} = 0.75\Delta\mu_{Bi}^X + 0.25\Delta\mu_{Sb}^0 + \Delta\mu_V^X + 4\Delta\mu_O^{Sb_2O_3} \tag{3.6}$$

Each term of equation 3.6 is varied with respect to the reference chemical species to form the FEL. In figure 3.5 the FEL governed by equation 3.6 is given. The entire triangle represents the range of free energies that promotes formation of the Sb_{Bi} doping configuration of BVO. The horizontal axis represents the change in Bi free energy and the vertical axis represents change in V free energy. The bisecting lines represents regions where the reference secondary phase is coexistent with Sb-BVO.

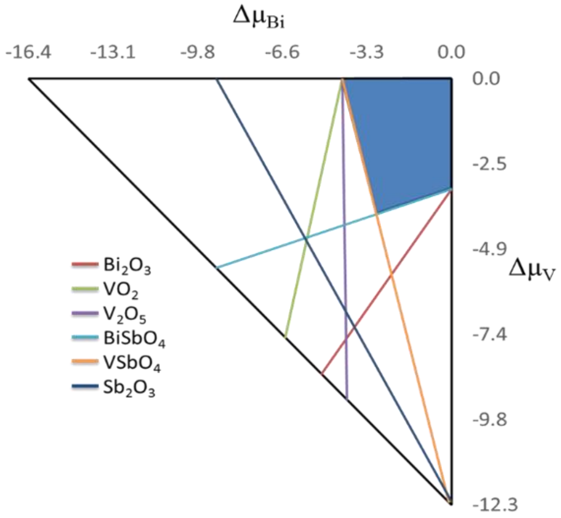

Figure 3.5 Free energy landscape of Sb-BVO. The axes are given in eV where the horizintal axis represents changes in Bi free energy and the vertical axis represents free energy changes for V. The entire triangle represents stable formation of Sb_{Bi}, the lines denoted by secondary phases represents regions where the reference secondary phase may form. The shaded region represents the range of free energies that promote the pure phase Sb-BVO.

The FEL approach is the primary tool to determine the existence of pure phase doping of a mixed metal oxide. In the following chapter we analyze a series of transition metal dopants in our prototype material and show how this information can be used to generate a probability distribution of different doping configurations.

Chapter 4

Bismuth Titanate (BTO)

4.1 Structural Properties of BTO

Bismuth titanate of the pyrochlore structure ($Bi_2^{3+}Ti_2^{4+}O_7$ abbrv. BTO), adopts Fd3m space group symmetry that has international tables number 227 and Schoenfiles name OH-7 [48]. This face centered cubic symmetry has two origin choices that are either (i) on an A cation or (ii) on a B cation (note, A = Bi and B = Ti) [40]. Construction of BTO is described as alternate stacking of triple layers of TiO_6 octahedra and monolayers of $(Bi_2O_2)^{2+}$ units along the c-axis [49]. In figure 4.1 a schematic view along a <111> direction of the cubic structure shows how $O'Bi_4$ tetrahedra interpenetrate corner connected TiO_6 octahedra in the pyrochlore structure. Experimental data consistently reports lattice parameters of BTO as, a = 10.298 Å ($\alpha = \beta = \gamma = 90°$) and the Ti-O, Bi-O, and Bi-O’ bond lengths as 1.964, 2.559, and 2.227 Å respectively [43–45]. The distinction between O and O’ atoms are based on their coordination with Bi atoms; O’ atoms have shorter bond lengths with Bi and are responsible for the activity of Bi 6s lone pair electrons. Our DFT results were in good agreement with a = 10.332 Å ($\alpha = \beta = \gamma = 90°$) and Ti-O, Bi-O, and Bi-O’ bond lengths at 1.982, 2.572, and 2.236 Å respectively. Our results also agree well with other theoretical results [36–40].

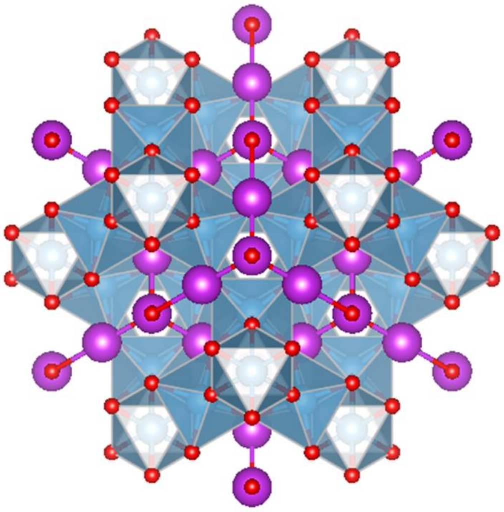

Figure 4.1: Schematic view of BTO dual type polyhedra along a <111> direction. The large, purple atoms are Bi atoms, the smaller, bluish atoms are Ti atoms, and the smallest red atoms are O atoms. The shaded regions of the structure are TiO_6 octahedral units while the un-shaded regions are the $O'Bi_4$ tetrahedral units. Bi-O bonds are not shown.

The stoichiometric pyrochlore is generally represented as $A_2^{3+}B_2^{4+}O_7$, but it has different charge balanced combinations as well ($A_2^{2+}B_2^{5+}O_7$ and $A_2^{1+}B_2^{6+}O_7$) [55–57]. Thus, further complex pyrochlore structures can be prepared by substitution of either A or B cations as long as they satisfy the ratio r_A/r_B = 1.29-2.30 Å (r = ionic radius) and maintain overall charge neutrality [58–60]. Interestingly, another feature of pyrochlore structures is summarized by the notation $A_2O'\cdot B_2O_6$, which basically represents how $O'A_4$ tetrahedra penetrate corner connected BO_6 octahedra [43,61]. This feature is the basis for accommodating frustrated magnetic spins in ice, glass, and liquid forms [62–65]. Also, when the A cation has lone pairs it displaces from its symmetric center in such a way the average structure retains its intrinsic phase [62,66–68].

4.2 Electronic Properties of BTO

In figure 4.2 the calculated electronic structure of pristine BTO pyrochlore shows how Bi 6s lone pairs form an antibonding state with O’ 2p electrons in the VBM. Deeper in the valence bands (not shown) is the bonding state that pushes the valence band closer to the CBM.

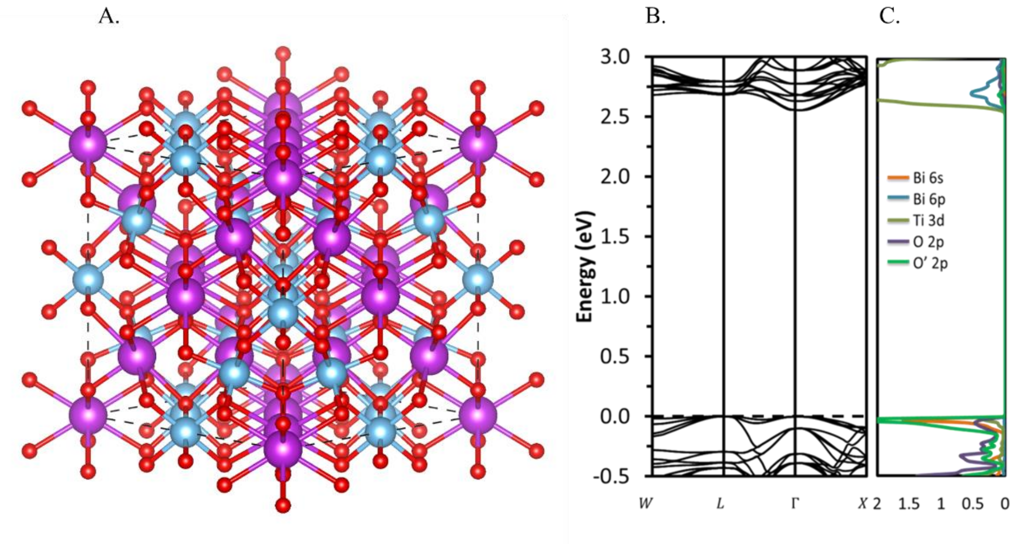

Figure 4.2: DFT calculated electronic structure of BTO. The band gap is shown to be approximately 2.6 eV at the Γ-point. The projected DOS shows that the VBM is composed of Bi 6s (lone pair) and O’ 2p antibonding level and the CBM is primarily Ti 3d the units are arbitrary.

This covalent nature of the A site network clearly plays an important role in the functionalization of BTO as a photocatalyst, therefore Bi atom substitutions are not typically considered [48,69,70]. Due to the atomic structure difference between transition metals and p-block cations, chemical intuition would dictate transition metals substitute transition metals. Here, however, the chance of a first row transition metal (TM) substituting either cation (A or B) as an impurity in BTO is possible. (i) TM in either cation site can achieve band gap reduction because d-electron ionization energies are typically slightly higher than that of the p-orbitals in BTO's VBM [48]. (ii) TM are typically terrestrially abundant ions with multiple valence states [71–75], thus charge neutrality can be achieved at either site. (iii) The ionic radii ratios for example, TM^{3+}/Ti^{4+} and Bi^{3+}/TM^{4+}, are between 1.29 and 1.98 respectively, which meet the r_A/r_B = 1.29-2.30 criteria.

4.3 Multi Metal Oxide Doping

4.3.1 Theoretical Context

From our theoretical perspective, further reduction of BTO's band gap via transition metal doping requires an electronic structure derived understanding of doping stability. In practice, a change to the chemical environment plays a significant controlling role on phase stability. If a priori knowledge of the effective conditions that control phase stability can be predetermined for any given case, it would be very beneficial to the quality of the materials we synthesize. Fortunately, thermodynamic modelling provides valuable information regarding free energy dependence of pure phase stability. Hence, state-of-the-art first principle methods like, density functional theory (DFT), are extremely useful for predicting the chemical parameters which govern pure phase synthesis of multi-metal oxides, or any other multicomponent material.

From this theoretical standpoint, TM substitutions in BTO or any other ternary metal oxide, could easily drive morphological phase transitions, among other detriments to the electronic structure, through a charge compensating mechanism. If we consider for example $\mathrm{Bi_{2-x}TM_xTi_2O_{7\pm y}}$ and $\mathrm{Bi_2Ti_{2-x}TM_xO_{7\pm y}}$ as two sets of probable doping configurations, where 'x' is independent and 'y' is dependent on the charge state of the TM ion, one can see how morphological phase transitions are driven. The simultaneous occurrence of O defects force cation/anion coordination changes which alter the notions that TM inclusion only increases n-type conductivity. Therefore, in this theoretical/computational study, we perform a phase stability analysis, with respect to O chemical potential, of two essential doping types based on A and B cation substitutions. The first types are first order configurations, substitutions of A and B cations, or TM_{Bi} and TM_{Ti} respectively. The second types are second order configurations defined as TM_{Bi} or TM_{Ti} coupled with an O vacancy or interstitial (TM_{Bi}-O_{vac}/O_{int} and TM_{Ti}-O_{vac}/O_{int}). Thus, evaluating the thermodynamic stability of these configurations should identify the doping configurations that lead to the formation of dopant inspired phases (DIP) in experiment.

4.3.2 Experimental Context

A peak in the photocatalytic performance of doped BTO has a corresponding pure phase vulnerability, especially for those grown using hydrothermal synthesis [13,15,22,76–83]. Hydrothermal synthesis is the go-to method for synthesizing single phase multi-metal oxides that depend on high pressure solubility of their precursors in hot water. Therefore density functional theory modelling is often overlooked due to its inability to address the associated kinetic effects, but pressure effects on the chemical environment can be modelled in many ways, including variation of the atomic free energies. For instance, in a growth process where O partial pressure is extremely reduced, stable configurations with X^{3+} cations may in some adiabatic process require reduction of the X cation to a 2+ charge state or, formations of O vacancies to compensate any charge imbalances. Such effects of low O partial pressure are modelled here by calculating the formation energy of X-doped $Bi_2Ti_2O_7$ (BTO) using a lower limit of available O free energy. Conversely, increased O partial pressure may require oxidation of the cation to a 4+ charge state or formations of O interstitials to accommodate a new charge distribution. This case is modelled here by calculating the formation energy of X-doped BTO using an upper limit of available O free energy.

4.3.3 FEL for BTO

From the analytical method described in the previous chapter we generated a constrained equation using the DFT calculated formation enthalpy of pristine BTO (equation 4.1). The superscripts are added to the generated constrained equation to indicate the referenced crystal phase and the source of additional free energies $\Delta\mu_i$.

$$\Delta H_f^{BTO} = -23.967 \text{ eV} = 7\Delta\mu_O^{BTO} + 2\,\Delta\mu_{Ti}^{BTO} + 2\Delta\mu_{Bi}^{BTO} \tag{4.1}$$

To test our free energy formalism we considered BTO precursors Ti_2O_3, Bi_2O_3 and TiO_2, then invoked O rich and poor conditions ($\Delta\mu_O = 0$ and $\Delta\mu_{O,min} = \Delta\mu_O^{BTO}$, respectively) on its formation enthalpy (see equations 4.2-4.4) to find the associated poor and rich coordinates of the given cation (either $\Delta\mu_{Bi}$ or $\Delta\mu_{Ti}$). Then the unknown cation free energy, $\Delta\mu_i$, was solved for by plugging the given values into the constrained equation. To obtain pure phase formation of BTO without any precursor phases the following inequalities had to be satisfied simultaneously. Each ΔH_f^X was derived from total energy calculations by using equation (4.1).

$$n_i\Delta\mu_i < \Delta H_f^{Ti_2O_3} = -14.129 \text{ eV} \tag{4.2}$$

$$n_i\Delta\mu_i < \Delta H_f^{Bi_2O_3} = -10.074 \text{ eV} \tag{4.3}$$

$$n_i\Delta\mu_i < \Delta H_f^{TiO_2} = -8.258 \text{ eV} \tag{4.4}$$

In figure 4.3, the chemical potential landscape formed by equation (4.1) shows that the boundary conditions could not be satisfied simultaneously in any region. Thus limiting the free energies with respect to BTO does not result in a single phase stability zone. This contradicts the many experiments [43,44,52,84,85] where single phase BTO was synthesized.

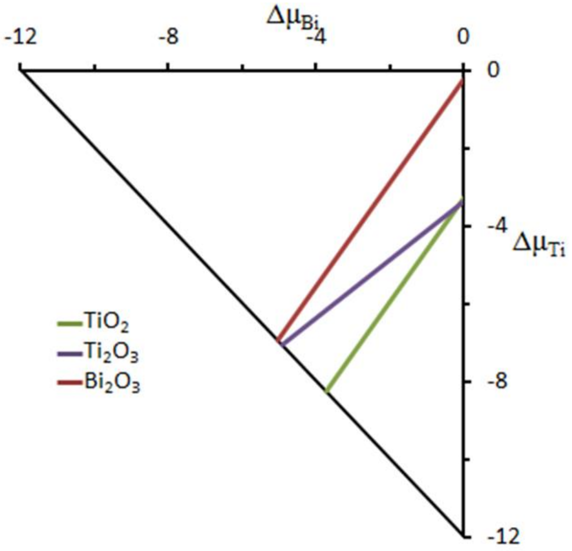

Figure 4.3 Chemical potential landscape of BTO in eV. Theoretically, due to improper bounding of $\mu_{O,min}$ the solution to the constrained equation contains cationic free energies that violate the upper bound limit. Experimentally, this would pertain to a crystalline solid that is composed of atoms with much kinetic energy, which is unphysical. Hence, no single phase region exists in this chemical potential landscape.

In experiment, the available free energies limits are the same for each phase but other conditions or kinetic effects may provide the required input of energy to promote the desired phase. Take for example hydrothermal synthesis of a mixed metal oxide [86–90], the partial pressures of constituent elements would depend on the high pressure solubility of the precursors in hot water. However, in a DFT calculation there is no such dependence on solubility or kinetics. If the lower limit of O free energy is defined with respect to ΔH_f^{BTO}, the value is too low to promote formation of all the considered precursors. For instance, to achieve the formation enthalpy of Bi2O3 using $\Delta\mu_{O,min} = \Delta\mu_O^{BTO}$, would require a $\Delta\mu_{Bi}^{Bi_2O_3}$ value that is greater than zero (i.e. $\Delta\mu_{Bi}^{Bi_2O_3} = {}^{1}/_{2}\,(-10.074 + {}^{3}/_{7} * 23.967) = 0.099$ eV), which is a direct violation of the predefined thermodynamic limits. Clearly then, the predictive power of our free energy formalism hinges on choosing limits for the $\Delta\mu_i$'s that abide by the rules. This is demonstrated further in the following chapter.

Chapter 5

Transition Metal Doped BTO

5.1 Introduction

Solar energy conversion methods, such as photovoltaic (PV) current production and photo-electrochemical (PEC) fuel production, require materials with high rates of photoexcited charge transfer from absorption of photons in the visible range of the electromagnetic spectrum. The challenge in developing such materials is to reduce the band gap by cation manipulation with minimal distortion of the underlying lattice symmetries. The potential enhancement of photocatalytic performance by doping tungstates [80,86,91–93], tantalates [77,94,95], vanadates [89,96,97,97], and titanates [49,93,93,98,99] has been rigorously studied. In ternary and higher order oxides, one of the major sources for poor response is the quality of the synthesized materials. It has been shown that it is highly challenging to synthesize a pure phase complex material, whether doped or pristine, due to likely formations of lower order oxides.

Bismuth titanate ($Bi_2^{3+}Ti_2^{4+}O_7$) with pyrochlore structure has been studied as a photocatalyst that can use solar energy to evolve hydrogen and oxygen gas (fuels) from water [51,85,92,100–104]. Popularity of BTO's water splitting ability is due to the fact it can be considered as an alloy of metal oxide photocatalysts Bi_2O_3 and TiO_2 (Bi_2O_3 + $2TiO_2 = Bi_2Ti_2O_7$). Since the band gap of TiO_2 straddles the redox potentials of water and Bi_2O_3 has a band gap of 2.8eV [13,105–108], the expectation of combining them to form BTO is the beneficial properties combine in such a way to form a better photocatalyst. For example, an expectation of BTO is its band gap should straddle the hydrogen and oxygen evolution potentials of water like TiO_2, and it should have conduction properties like Bi_2O_3 and other Bi containing oxides making amphoteric, which is a property needed to evolve both fuels in one-step. However, the band gap of BTO is not much smaller than its parent oxides at around 2.8eV [48,51], even though its valence band maximum (VBM) is higher than both Bi_2O_3 and TiO_2 according to our calculated O 1s core levels. Ultimately, the band gap and band edge alignments of BTO prevent it from being more active in visible light, but there is potential to increase its efficiency as a water-splitter provided its limitations can be overcome with doping.

In this chapter we embrace the opportunity to increase our electronic understanding of doping stability in BTO. The free energies derived from our DFT calculations are analyzed to determine the chemical potential ranges that promote single phase stability of Cr, Mn and Fe doped BTO. A systematic study of different doping configurations along with their electronic structures will be given. We answer questions like: Which cation site is most probable to be substituted by the dopants? Do any intrinsic defects like O vacancies or interstitials accompany stable doping? We explore onsite interactions at the A and B-site upon doping by using charge density difference plots and we offer a discussion of our theoretical results with respect to selected experiments found in the literature.

5.2 Experimental Context

Recently, iron doped BTO (Fe-BTO) was hydrothermally synthesized using a surfactant assisted wet chemical reverse micelle-based method [36,109]. The synthesized Fe-BTO samples had a band gap that was reduced in comparison to regular BTO, but the photocurrent decreased with higher Fe concentrations. Coexistence of Fe_2O_3 was confirmed at a Fe concentration around 2 wt. %, which was marked as the detriment to photoconduction. In principle, thermodynamic changes within the high pressure autoclave could have contributed to this pure phase vulnerability. For instance,

$BiCl_3$ was allowed to flow in to the autoclave as an effort to address evaporation of Bi atoms. Sourcing Bi atoms with $BiCl_3$ has proven success in the synthesis of Bi containing oxides using the chemical vapor deposition (CVD) and solid-liquid-solid (SLS) methods [110–115] however, these methods are done at low pressure whereas hydrothermal synthesis is done at high pressure. Furthermore, $BiCl_3$ is a halide known for its own catalytic properties [116–118] that could cause local reduction of the cations in multi-metal oxides apart from the varying O free energy.

Mn-BTO particles were recently synthesized using a similar technique as in reference 23 [53]. The authors reported that around 1% doping concentration, Mn-BTO samples showed band gap reduction of about 0.4 eV and the peaked H_2 evolution rate was twice that of the Fe-BTO samples. Since the Mn-BTO particles were about 20nm smaller than the Fe-BTO particles, the increase in photocatalytic performance was attributed to size effects. Indeed, within a size regime where the exciton radius is greater than one of the particle’s dimensions, shorter charge diffusion lengths and larger reaction sites are expected. However, in terms of phase stability, larger crystals are preferable.

An experimental study on Cr-doped bismuth titanate has also been done but with different stoichiometric BTO [119]. $Bi_4Ti_3O_{12}$ was synthesized as nano-sheets from another facile hydrothermal approach which they claim had a high percentage of reactivity on {110} facets. They attribute enhanced visible-light absorption to the presence of Cr 2p levels in the VBM, and claim to have doped Cr in BTO up to a concentration of 2.1 wt. % ($Bi_4Ti_{3-x}Cr_xO_{12}$ with x = 0.4) before the photocatalytic performance reduced. Based on XRD and XPS, the authors concluded that a change in the redox potential of Cr ions caused a reduction in photocurrent.

5.3 Model Application

The following constrained equations represent free energy dependent formation of the secondary phases (precursors and DIPs) related to A-site, X = Cr, Mn or Fe, doping in BTO.

$$\Delta H_f^{X_{Bi}} = 7\Delta\mu_O + 2\Delta\mu_{Ti} + 1.875\Delta\mu_{Bi} + 0.125\Delta\mu_X \tag{5.1}$$

$$\Delta H_f^{Bi_2O_3} = 3\Delta\mu_O^{Bi_2O_3} + 2\Delta\mu_{Bi}^{X_{Bi}} \tag{5.2}$$

$$\Delta H_f^{TiO_2} = 2\Delta\mu_O^{TiO_2} + \Delta\mu_{Ti}^{X_{Bi}} \tag{5.3}$$

$$\Delta H_f^{BiXO_3} = 3\Delta\mu_O^{X_2O_3} + \Delta\mu_{Bi}^{X_{Bi}} + \Delta\mu_X \tag{5.4}$$

$$\Delta H_f^{XTiO_3} = 3\Delta\mu_O^{X_2O_3} + \Delta\mu_{Ti}^{X_{Bi}} + \Delta\mu_X \tag{5.5}$$

$$\Delta H_f^{X_2O_3} = 3\Delta\mu_O^{X_2O_3} + 2\Delta\mu_X \tag{5.6}$$

Equation 5.1 is the governing equation that generates the chemical potential landscape for X-doped BTO. Equations 5.2 and 5.3 represent formation of precursor oxides that could source Bi and Ti ions. Equations 5.4 and 5.5 represent formation of DIPs that are dependent on $\Delta\mu_{Bi}$ and $\Delta\mu_{Ti}$ and equation 5.6 represents formation of a DIP that is independent of $\Delta\mu_{Bi}$ and $\Delta\mu_{Ti}$. Each of these linear equations introduces further constraints on the chemical potentials that empower us to analyze the effects of free energy changes given any coupling condition.

In experiment, coupling conditions can be considered in many different ways, however, for brevity we will only consider two different cases in this study, (i) formation of a secondary phase coupled only with X doped BTO, and (ii) formation of a secondary phase coupled with X doped BTO and the other secondary phases. For case (i) formation, a simultaneous system of equations can be made out of equations 5.1 and 5.2 (if we are considering simultaneous Bi_2O_3 formation). Then we imposed a constant X-rich condition and invoked the O rich and poor conditions ($\Delta\mu_{O} = 0$ and $\Delta\mu_{O} = \Delta\mu_{O,min}$, respectively). According to equation 5.2, when $\Delta\mu_{O} = 0$ the value of $\Delta\mu_{Bi} = \Delta H_f^{Bi_2O_3}/2$, which is the Bi poor condition with respect to Bi_2O_3. Now when $\Delta\mu_{O} = \Delta\mu_{O,min}$, we were simultaneously considering the Bi rich condition, $\Delta\mu_{Bi} = 0$ and according to Equation (6), $\Delta\ \Delta\mu_{O,min} = \Delta H_f^{Bi_2O_3}/3$ which is the O poor condition with respect to Bi_2O_3. The unknown $\Delta\mu_{Ti}$ for O poor and O rich was solved for by plugging the respective $\Delta\mu_{Bi}$ and $\Delta\mu_{O}$ pairs into equation 5.1. In a similar fashion, the other secondary phase boundaries were determined.

5.4 Cation Doping

In table 5.1 we show the structural properties for all three dopants X = Cr, Mn and Fe at the A and B-cation sites from our calculations.

Table 5.1 Cell parameters (Å), lattice angles (degrees), cell volume (Å^3), and mean bond lengths (Å) for dopants X = Cr, Mn or Fe in pristine BTO at the A and B cation sites.

Species	**a**	**α**	**B**	**γ**	**V**	**Bi-O**	**Ti-O**	**X-O**
BTO	10.330	90.000	90.000	90.000	1102.156	2.486	1.982	
Cr$_{Bi}$	10.328	89.933	90.067	90.067	1101.610	2.440	1.978	1.813
Cr$_{Ti}$	10.348	89.881	90.119	90.119	1108.065	2.412	1.982	1.954
Mn$_{Bi}$	10.324	89.907	90.093	90.093	1100.421	2.439	1.978	1.793
Mn$_{Ti}$	10.347	89.868	90.132	90.132	1107.792	2.413	1.982	1.942
Fe$_{Bi}$	10.327	89.948	90.053	90.053	1101.471	2.441	1.978	1.813
Fe$_{Ti}$	10.345	89.875	90.125	90.125	1106.961	2.411	1.982	1.928

It can be seen for each doping case, the lattice parameters are indicative of an overall cubic structure. The listed cell volumes however, show that dopants at the A-site had negligible effects on the cell's volume while dopants at the B-site caused considerable expansions of it. For Cr doping at the A-site (Cr$_{Bi}$), the Cr ion is mainly bonded to two O' atoms each with a bond length of 1.813 Å, whereas the six O atoms surrounding the Cr ion were all 2.590 Å away. Compared to the Bi-O' bond length of pristine BTO (2.236 Å), the Cr$_{Bi}$-O' bond length was a reduction of about 19%; a significant reduction due to the smaller atomic size of Cr compared to Bi. However, the Ti-O bonds associated with this structure ranged from 1.893 to 2.086 Å (a mean of 1.978 Å); a 0.2% reduction from that of pristine BTO (1.982 Å). This shows that distortions from Bi substitutions can be compensated locally. On the other hand, for Cr doping at the B-site (Cr$_{Ti}$), the Cr ion is bonded to six O atoms that each have a bond length of 1.954 Å. Compared to the Ti-O bond length of pristine BTO (1.982 Å), this is a reduction of about 1.5%. However, the Bi-O bonds associated with this structure ranged from 2.242 to 2.578 Å (a mean of 2.412 Å), so the Bi-O' bonds did not change much whereas the Bi-O bonds increased more than 4%. This shows that distortions caused by Ti-site doping are distributed over both cation sublattices. The trend is similar for Mn and Fe doping. For Mn_{Bi} the six O atoms surrounding the Mn atom are all 2.578 Å away and the two O' atoms have bond lengths of 1.793 Å, about a 20% reduction from pristine Bi-O' bond lengths. The Ti-O bonds in this structure ranged from 1.897 to 2.081 Å (a mean of 1.978 Å), about a 1% reduction from pristine Ti-O bond lengths. For Mn_{Ti} the six surrounding O atoms are 1.942 Å away. The Bi-O bonds associated with this structure ranged from 2.241 to 2.578 Å (a mean of 2.413 Å). Lastly, for FeBi, the six surrounding O atoms are 2.598 Å away and the two O' atoms have bond lengths that are 1.813 Å. The Ti-O bonds associated with this structure range from 1.893 to 2.085 Å (a mean of 1.978 Å). For Fe_{Ti} the six surrounding O atoms have bond lengths that are 1.927 Å. The Bi-O bonds associated with this structure range from 2.242 to 2.578 Å (a mean of 2.411 Å).

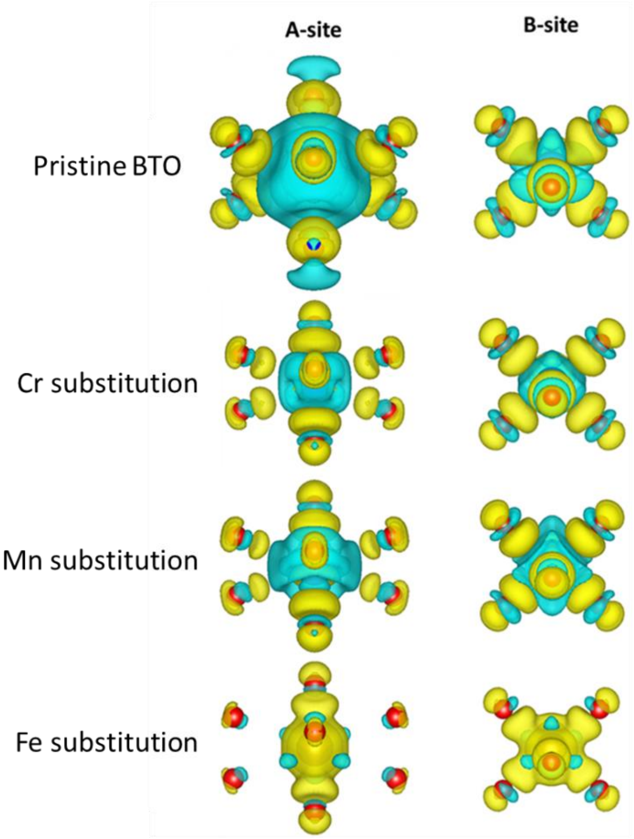

Figure 5.1 Charge density differences for A and B cation sites for pristine BTO, Cr-BTO, Mn-BTO, and Fe-BTO. The isosurface levels are the same value in each case. Fe shows a significant orbital overlap in comparison to Cr and Mn.

In figure 5.1, the charge density difference plots, $\Delta\rho_{\mathrm{AB}}$, for pristine BTO and X = Cr, Mn, and Fe doped BTO in A and B-sites are given. It can be seen from the A-site doping that the central dopant atom increases its orbital overlap with O' atoms and reduces its ionic components with O atoms, as table 5.1 suggests. From the B-site doping column not much orbital overlap can be seen except in the Fe doping case where the overall bonding polyhedra gets smaller. Summarily, X_{Bi} doping configurations demonstrated the least amount of distortions in comparison to X_{Ti} doping configurations. The associated Ti-O and Bi-O bonds were virtually unchanged, but in the X_{Bi} cases X-O' was always a reduction in comparison to the Bi-O' bonds of pristine BTO. As was pointed out in the X_{Bi} case, the A-site is a 'distortion-tolerate site' because of its bonding with the O' atoms which are not shared with Ti atoms. Hence, for X_{Bi} the distortion is mainly along X-O' bonds. On the other hand, Ti atoms are bonded with O atoms which are also shared by Bi atoms, so distortions at this site effect both sublattices.

In reference 108, the authors discuss their Cr 2p fine XPS spectra, and based on the difference between their observed binding energy (576.3 eV) and a reported [120] Cr^{3+} binding energy (577.6 eV), they suggest at the low Cr concentrations they considered, Cr ions have predominantly 4+ charge states and therefore sit at Ti-sites. In an experimental study of the XPS spectra of first row transition metals, a controversy between binding energies of Cr^{3+} and Cr^{4+} [121] is discussed. It was stated that, due to the overlapping of fine multiplet Cr^{3+} spectra with singlet Cr^{6+} spectra, false readings for Cr^{4+} are common. Furthermore, authors from another experimental study on the photo-reduction of hexavalent Cr by XPS measurements found the fitting parameters for Cr^{3+} and Cr^{4+} to be 576.3 eV and 575.2 eV, respectively [122], therefore reference 108 may be an instance of a false reading. From our results, shown in table 5.1, X_{Ti} doping corresponds to a slight increase in the lattice parameters whereas X_{Bi} doping corresponds to little or no change in the lattice parameter. Therefore one can expect the characteristic XRD peaks of X-doped BTO to either shift to lower angles in the case of X_{Ti} doping or remain the same in the case of X_{Bi} doping. In figure 1, of reference 23, the characteristic XRD peaks of the assumed Cr_{Ti} doping virtually stay the same with increasing Cr doping and in figure 3 of reference 108, the characteristic XRD peaks shifted to higher angles.

In figure 5.2 A), the chemical potential landscapes representing case (i) formation of the secondary phases is shown and the following inequalities represent the range of chemical potentials that avoid their formation. Our calculated value for each formation enthalpy is given in table 5.2 as a reference.

$$\sum_i n_i \Delta\mu_i < \Delta H_f^{Bi_2O_3} \tag{5.7}$$

$$\sum_i n_i \Delta\mu_i < \Delta H_f^{TiO_2} \tag{5.8}$$

$$\sum_i n_i \Delta\mu_i < \Delta H_f^{BiXO_3} \tag{5.9}$$

$$\sum_i n_i \Delta\mu_i < \Delta H_f^{XTiO_3} \tag{5.10}$$

$$\sum_i n_i \Delta\mu_i < \Delta H_f^{X_2O_3} \tag{5.11}$$

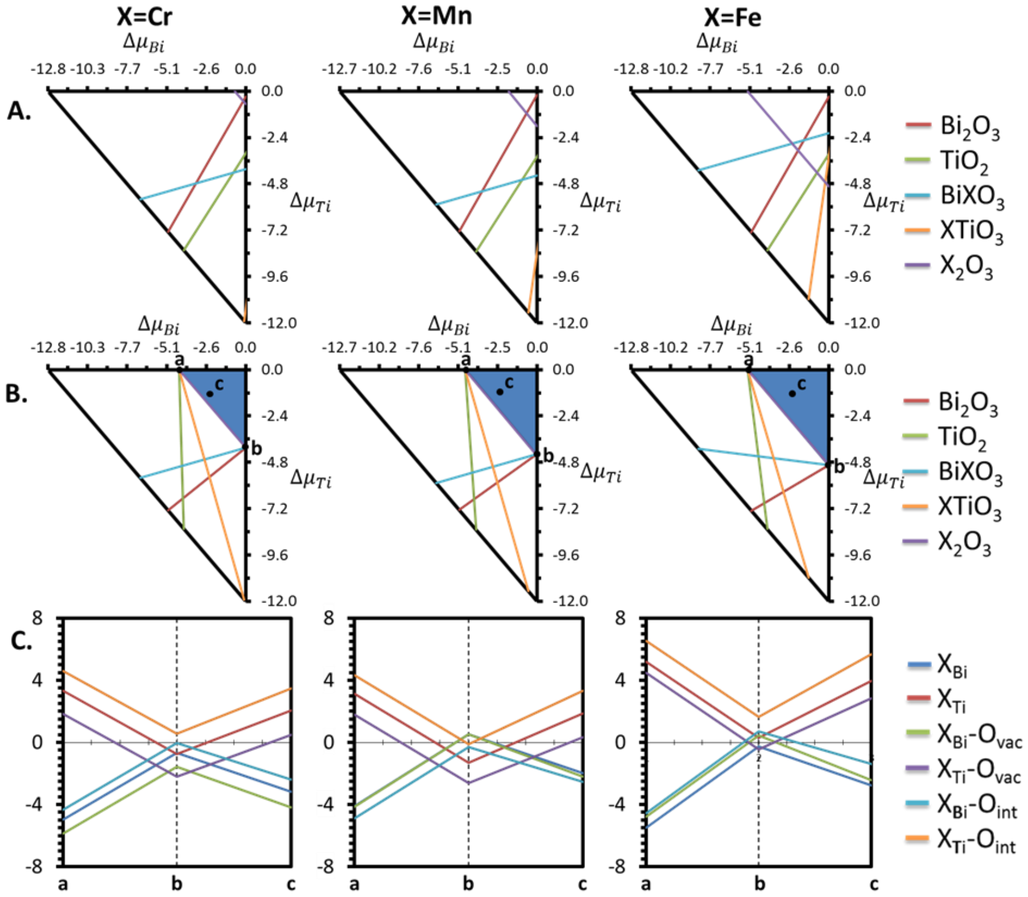

Figure 5.2 Stability analysis of X = Cr, Mn and Fe doping in BTO. A.) are the chemical potential landscapes that represent case (i) formation of secondary phases. B.) are the chemical potential landscapes that represent case (ii) formation of secondary phases and C.) are the defect formation energy distributions with respect to the points **a** = the $\Delta\mu_{\mathrm{Bi}}$-intercept or Ti-rich triple point, **b** = $\Delta\mu_{\mathrm{Ti}}$-intercept or Bi-rich triple point, and **c** = (-2.50,-1.25) of the corresponding chemical potential landscape. All scales are in eV.

Table 5.2 Calculated formation energies in eV. For each dopant X = Cr, Mn, Fe, the A-site substitution is shown as it is the most stable substitution site for all dopants. Bismuth oxide and titanium dioxide are the dopant independent secondary phases considered. Other phases are dopant and Bi/Ti dependent secondary phases and dopant Bi/Ti independent phases. For X = Cr and Mn, $BiXO_3$ has the highest formation energy and for X = Fe, X_2O_3 has the highest formation enthalpy.

Phase	**X=Cr**	**X=Mn**	**X=Fe**
X_{Bi}	-24.050	-23.900	-23.998
Bi_2O_3	-10.074	-10.074	-10.074
TiO_2	-8.258	-8.258	-8.258
$BiXO_3$	-6.845	-6.510	-8.455
$XTiO_3$	-11.941	-11.428	-10.761
X_2O_3	-9.726	-8.773	-6.072

Apparently, case (i) formation does not allow single phase formation of X doped BTO, due to the fact each phase has its own range of $\Delta\mu_O$ which may not be suitable to form the other phases. According to our inequalities if a chemical potential is too low the referenced secondary phase cannot form. Take for example $\Delta\mu_{O,min} = \Delta H_f^{TiO_2}/2$, which equals -4.129 eV, at this O-poor condition, X-doped BTO itself cannot even form because $\Delta\mu_{O,min} = \Delta H_f^{X_{Bi}}/7$ is always greater than -4.129 eV (note Bi_2O_3 and TiO_2 boundary lines are parallel in each case).

Now for case (ii) formation we make a simultaneous system of equations out of equations (5.1) and (5.2) (that is considering the formation of Bi_2O_3 as an example again) and the equation that represents formation of the least stable secondary phase (e.g. the one that has the largest formation enthalpy). So, for X = Cr or Mn, equation (5.4) is considered and for X = Fe, equation (5.6) is considered. In figure 5.2 B), the chemical potential landscapes representing case (ii) formation are shown. Notice how the Bi_2O_3 and TiO_2 boundary lines are now perpendicular in each case. According to the inequalities (equations 5.7-5.11), single phase formation of X doped BTO emerges as the area bounded by $\Delta\mu_{O,min}$ and the $\Delta\mu_{Bi}/\Delta\mu_{Ti}$ axes (the shaded area). Choosing to define $\Delta\mu_{O,min}$ with respect to the least stable phase promotes formation of BTO and all secondary phases. It is worth mentioning here that only one independent DIP (X_2O_3) boundary is shown while other independent DIP boundaries are not shown. This is due to the fact different binary X-oxides will not coexist in the same plane as defined in figure 5.2 B). For example, lines representing Mn_2O_3, MnO_2 and $BiMnO_3$ cannot exist in the same plane where Mn-BTO is stable at thermodynamic equilibrium; Mn_2O_3 and $BiMnO_3$ will co-exist in one plane (as shown here) and MnO_2 and $BiMnO_3$ will exist in another plane (not shown here).

The case (ii) formation picture produces chemical potential landscapes that are easily correlated to experiment. For example, the small region in figure 5.2 B) where Bi_2O_3 and TiO_2 are coexistent with BTO, can be correlated to the chemical parameters of reference 108 where stable $Bi_4Ti_3O_{12}/Bi_2Ti_2O_7$ (note: $Bi_4Ti_3O_{12} = Bi_2Ti_2O_7 + Bi_2O_3 + TiO_2$) was formed. According to the authors, when the Cr wt. % was increased, the heterostructure became predominantly $Bi_2Ti_2O_7$. Correlating this observation with our DFT results, one can easily determine there is a free energy dependence between Cr and O ions. Since the pure phase zone is along the direction of reducing O free energy we can predict pure phase Cr-doped BTO should be done in O-poor conditions.

From figure 5.2 B), we chose the points **a**, **b**, and **c** because of their relationship to chemical parameters that can be controlled in experiment. Point **a** is the $\Delta\mu_{Bi}$-intercept/Ti-rich condition, three Ti-related secondary phases converge to this point. Point **b** is the $\Delta\mu_{Ti}$-intercept/Bi-rich condition and point **c** has coordinates in the ($\Delta\mu_{Bi}$, $\Delta\mu_{Ti}$)-

plane equal to (-2.5,-1.25) eV. This coordinate pair was taken to represent a Bi/Ti ratio less than 1, as A-site doping is more stable than B-site doping in general according to our formation enthalpy calculations (not shown here explicitly). Figure 5.2 C) shows the formation energies of first and second order X doping configurations with respect to points **a**, **b** and **c**; the linear expression for defect formation energy is given by equation (3.2). The first order configurations are, for example, substitutions of A and B cations or X_{Bi} and X_{Ti}, respectively. The second types are second order configurations defined as X_{Bi} or X_{Ti} coupled with an O vacancy or interstitial (X_{Bi}-O_{vac}/O_{int} and X_{Ti}-O_{vac}/O_{int}). Positive formation energies indicate endothermic reactions that require an input of energy and thus are less likely to form. Negative formation energies indicate exothermic reactions that form spontaneously and thus are more likely to form. At first glance it can be seen that A-site doping are exothermic reactions while B-site doping are endothermic reactions with respect to points **a** and **c**. At point **b**, A and B-site doping transition to endothermic and exothermic reactions respectively. Hence, only when the Ti condition is its poorest does X_{Ti} doping become favorable in comparison to X_{Bi} doping.

From our formation enthalpy calculations the most favorable doping configurations for X = Cr, Mn and Fe are X_{Bi}-O_{vac}, X_{Bi}-O_{int}, and X_{Bi}, respectively. These are also the most favorable doping configurations with respect to points **a** and **c** of our FELs. Likewise, the least favorable doping configuration in terms of formation enthalpy is X_{Ti}-O_{int} for all dopants, which happens to be the most favored doping configuration for all dopants at point **b**. This suggests X_{Ti} and O_{int} related doping, which are promoted in Ti-poor and O-rich conditions, correspond to formations of secondary phases.

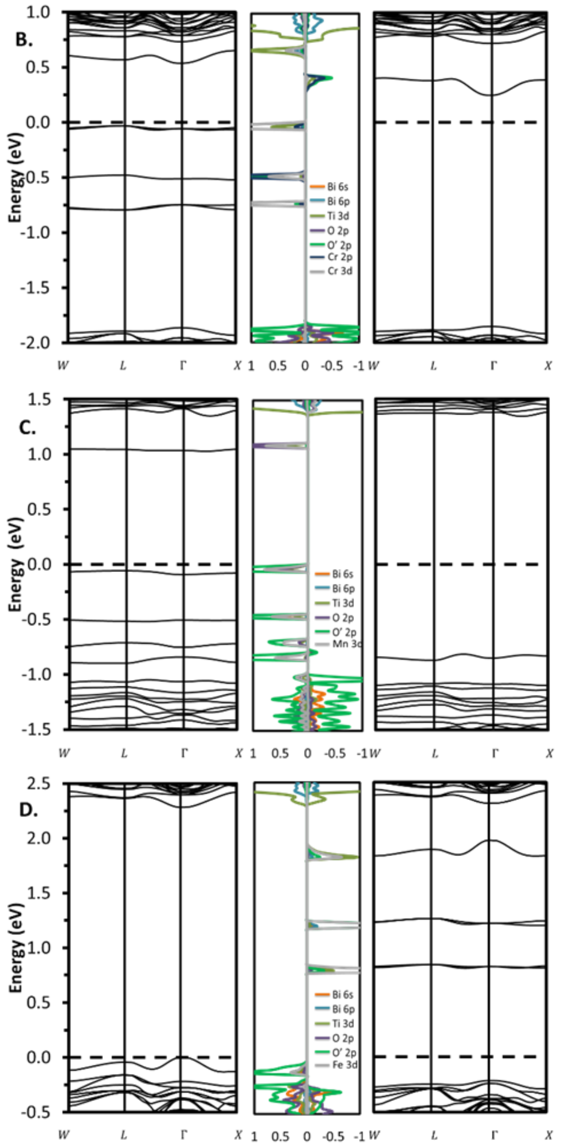

Figure 5.3 GGA determined electronic structures for the most favorable X doping configurations per the free energy landscape. A) BTO, B) Cr$_{Bi}$-O$_{vac}$, C) Mn$_{Bi}$-O$_{int}$, and D) Fe$_{Bi}$. FCC Brillouin zone was used to specify symmetric points in the lattice. The left panel represents the majority channel and the right panel (if shown) represents the minority channel. The center panels are the site projected partial density of states.

In figure 5.3 we show the electronic structures of A) pristine BTO, B) Cr_{Bi}-O_{vac}, C) Mn_{Bi}-O_{int} and D) Fe_{Bi} which are the most favorable conditions with respect to point **c** of the chemical potential landscapes. In figure 5.3 (A), the electronic structure shows that Bi 6s lone pairs form an antibonding state with O' 2p electrons at the VBM. The band gap is approximately 2.6 eV direct at the Γ-point. Deeper in the valence bands (not shown), the Bi 6s + O' 2p bonding state pushes the valence band closer to the CBM. The CBM at the Γ-point shows a dispersive electronic state that is indicative of electrons with reduced effective mass in the first brillouin zone.

In figure 5.3 (B), the spin polarized, GGA calculated electronic structure of Cr_{Bi}-O_{vac} is shown. The band structure shows both occupied and unoccupied mid gap bands that are virtually dispersion-less in the majority channel. Irrespective to these mid gap states the band gap is about 2.5 eV at the Γ-point. The PDOS shows that these mid gap bands have both Cr 2p and Cr 3d character but the 3d character is more dominant. The highest occupied mid gap state also has Ti 3d character which suggest some cation-cation interactions. This may be due to the fact, O' states are reduced, given an O_{vac}. In the minority channel the band gap measured from the VBM to the one unoccupied mid gap band is about 2.3 eV at the Γ-point and measured to the CBM it is 2.5 eV. The PDOS shows that the unoccupied mid gap band is mostly composed of Cr and O' 2p levels.

In Figure 5.3 C), the spin polarized, GGA calculated electronic structure of Mn_{Bi}-O_{int} is shown. The band structure of the majority channel shows both occupied and unoccupied mid gap bands composed of Mn 3d + O' 2p. However, due to their dominant 3d character, they are very flat which indicates effective hole masses would be too massive for enhanced photoconduction. Nonetheless, the band gap measured from the VBM to the CBM between the Γ- and L-points is about 2.3 eV. In the minority channel the band gap is about 2.1 eV measured from the one occupied mid gap band to the CBM between the Γ- and L-points. From the VBM to CBM the band gap is about 2.3 eV. The PDOS shows that the composition of the VBM and the occupied mid gap state are mostly O’2p. This may be due to the fact more O’ 2p states are available, given an O_{int}.

In Figure 5.3 D), the spin polarized, GGA calculated electronic structure of Fe_{Bi} is shown. In the band structure for the majority channel, mid gap states are absent and the band gap is about 2.3 eV, direct at the Γ-point. The VBM is predominantly O’ 2p-like, and the CBM is Ti 3d-like. In the minority channel there resides five unoccupied mid gap bands. Irrespective to these mid gap bands the band gap is about 2.5 eV.

5.5 Fe Substitutions

We obtained the GGA-DFT determined, energy dependent, dielectric function of each doping configuration in order to simulate their optical absorption. In Figure 5.4, a plot of the simulated optical absorption is shown. For wavelengths greater than 490 nm (shown by inset), each Fe doping configuration absorbs more visible light than pristine BTO, indicating Fe doping in general reduces the optical gap.

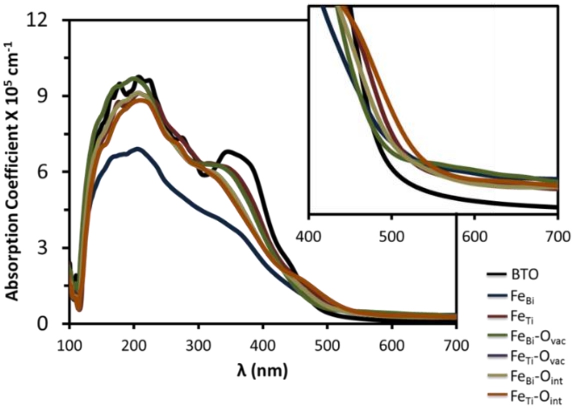

Figure 5.4 Simulated spectral absorption of pristine BTO and all of the first and second order Fe doping configurations. The inset is a magnification of the optical absorption over the range of visible light. Red shifted absorption is shown for all Fe doping configurations. Fe_{Bi} and Fe_{Bi}-O_{vac} have the greatest increase in optical absorption over all.

At around 553 nm to 700 nm, Fe_{Bi} and Fe_{Bi}-O_{vac} are shown to be the most absorptive. This indicates that Fe_{Bi} related doping is more favorable for absorption of photons in the visible range than Fe_{Ti} related doping. In figure 5.5 the constant charge density differences ($\Delta\rho$) are shown for Fe_{Bi} and Fe_{Ti} next to their respective $\Delta\rho$ of the A and B cation sites in pristine BTO.

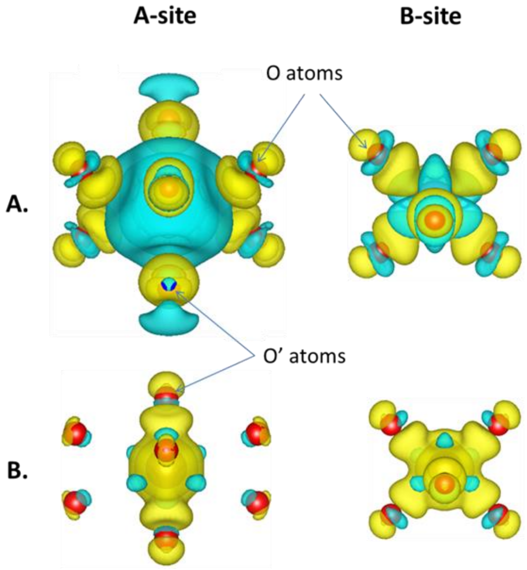

Figure 5.5 Charge density difference of A) pristine BTO projected at the A (Bi) and B (Ti) sites and B) Fe doped BTO projected at the A and B-sites. Both site substitutions show increased covalent content of their respective bonding polyhedra. However in the Fe_{Bi} case covalency is increased with O' atoms only where as in the Fe_{Ti} case the entire octahedral is affected.

It can be seen that when Fe replaces a Bi atom the site interactions with O' atoms increase while the interactions with O atoms are unchanged. This indicates the covalent network adjusts to accommodate the dopant and prevents distortion of the surrounding bonding polyhedra. In figure 5.5 it is shown that Fe substitution of Ti completely changes the nature of the bonding from ionic to covalent. This undoubtedly distorts the surrounding polyhedra promoting morphological transitions.

To further demonstrate how critical it is to choose the proper limits, we chose limits based on empirical evidence to derive the chemical potential landscape of Fe-BTO. In figure 5.6 we show the free energy landscape formed by generating a constrained equation with respect to Fe_{Bi} (equation 5.12).

$$\Delta H_f^{Fe_{Bi}} = -23.998\ \mathrm{eV} = 7\Delta\mu_O^{Fe_2O_3} + 2\Delta\mu_{Ti}^{Fe_{Bi}} + 1.875\Delta\mu_{Bi}^{Fe_{Bi}} + 0.125\Delta\mu_{Fe} \tag{5.12}$$

Since Fe_2O_3 formation was observed in reference 23, we considered some possible Fe DIPs (equations 5.13 and 5.14) and defined $\Delta\mu_{O,min}$ with respect to Fe_2O_3.

$$n_i\Delta\mu_i < \Delta H_f^{Fe_2O_3} = -6.072\ \mathrm{eV} \tag{5.13}$$

$$n_i\Delta\mu_i < \Delta H_f^{BiFeO_3} = -9.182\ \mathrm{eV} \tag{5.14}$$

By quick inspection of equations 5.7-5.11 one can see that $\Delta\mu_{O,min}$ with respect to Fe_2O_3 has the highest value for O poor condition among all of the considered precursors and DIPs. Hence, by using $\Delta\mu_O^{Fe_2O_3}$ as the limiting value for $\Delta\mu_{O,min}$, the rules pertaining to the thermodynamic limits are maintained. As a result, all of the boundary conditions are found to be satisfied simultaneously in the shaded region shown in figure 5.6. Each coordinate within this region represents a set of free energies that will result in a pure phase of Fe-BTO.

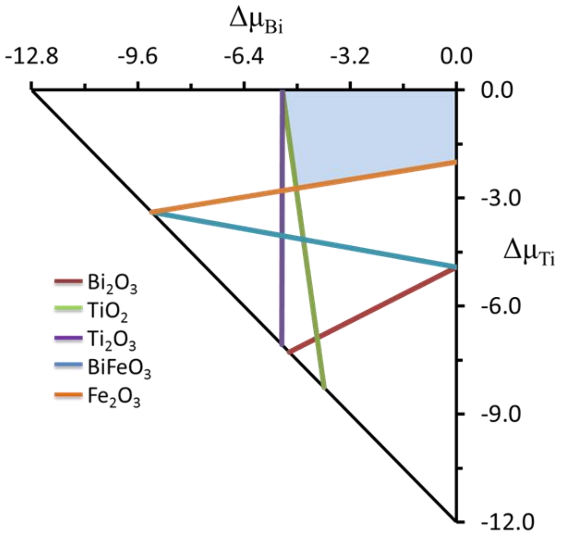

Figure 5.6 Chemical potential landscape of Fe_{Bi} by properly limiting the availability of O free energy. The single phase stability zone for Fe_{Bi} is indicated by the shaded region. The corners of the triangle were determined by imposing the associated O rich/poor conditions on the host formation enthalpy. The universal O rich condition is along the diagonal line and the O poor condition is at the origin.

Synergy between $\Delta\mu_{Bi}$ and $\Delta\mu_{Ti}$ is more evident if we consider constrained equations 5.15 and 5.16,which are generated with respect to two consecutive Fe doping concentrations, $Bi_{1.875}Fe_{0.125}Ti_2O_7$ (1 Fe atom per BTO unit cell) and $Bi_{1.75}Fe_{0.25}Ti_2O_7$ (2 Fe atoms per BTO unit cell) where $\Delta\mu_{Bi}$, $\Delta\mu_{Fe}$ and $\Delta\mu_{O}$ are fixed (following the experimental condition).

$$\Delta H_f^{Fe_{Bi}} = 7\Delta\mu_O + 2\Delta\mu_{Ti}^{Fe_{Bi}} + 1.875\Delta\mu_{Bi} + 0.125\Delta\mu_{Fe} \tag{5.15}$$

$$\Delta H_f^{2Fe_{Bi}} = 7\Delta\mu_O + 2\Delta\mu_{Ti}^{2Fe_{Bi}} + 1.75\Delta\mu_{Bi} + 0.25\Delta\mu_{Fe} \tag{5.16}$$

From manipulation of these equations it is seen that $\Delta\mu_{Ti}$ is characteristic.

$$\Delta\mu_{\mathrm{Ti}}^{\mathrm{Fe_{Bi}}} = \left(\Delta\mathrm{H}_{\mathrm{f}}^{\mathrm{Fe_{Bi}}} - 7\Delta\mu_{\mathrm{O}} - 1.875\Delta\mu_{\mathrm{Bi}} - 0.125\Delta\mu_{\mathrm{Fe}}\right)/2 \qquad (5.17)$$

$$\Delta\mu_{\mathrm{Ti}}^{\mathrm{2Fe_{Bi}}} = \left(\Delta\mathrm{H}_{\mathrm{f}}^{\mathrm{2Fe_{Bi}}} - 7\Delta\mu_{\mathrm{O}} - 1.75\Delta\mu_{\mathrm{Bi}} - 0.25\Delta\mu_{\mathrm{Fe}}\right)/2 \qquad (5.18)$$

Then by computing the difference between $\Delta\mu_{\mathrm{Ti}}^{\mathrm{2Fe_{Bi}}}$ and $\Delta\mu_{\mathrm{Ti}}^{\mathrm{Fe_{Bi}}}$ we get an interesting relationship, which we define the doping correlation energy.

$$\Delta\mu_{\mathrm{Ti}}^{\mathrm{2Fe_{Bi}}} - \Delta\mu_{\mathrm{Ti}}^{\mathrm{Fe_{Bi}}} = \left[\left(\Delta\mathrm{H}_{\mathrm{f}}^{\mathrm{2Fe_{Bi}}} - \Delta\mathrm{H}_{\mathrm{f}}^{\mathrm{Fe_{Bi}}}\right) + 0.125(\Delta\mu_{\mathrm{Bi}} - \Delta\mu_{\mathrm{Fe}})\right]/2 \qquad (5.19)$$

Equation 5.19 suggests two points: (i) at the Fe rich condition, $\Delta\mu_{\mathrm{Ti}}$ will depend linearly on $\Delta\mu_{\mathrm{Bi}}$, and (ii) $\Delta\mu_{\mathrm{Ti}}$ with two $\mathrm{Fe_{Bi}}$ in BTO is lower (more negative) than $\Delta\mu_{\mathrm{Ti}}$ with one $\mathrm{Fe_{Bi}}$. That is to say, at a fixed $\Delta\mu_{\mathrm{Bi}}$, a higher frequency of $\mathrm{Fe_{Bi}}$ would decrease $\Delta\mu_{\mathrm{Ti}}$. From Figure 5, it is evident that lower $\Delta\mu_{\mathrm{Ti}}$ would promote the formation of Fe_2O_3, which corresponds to the experimental scenario where beyond the Fe doping threshold formation of Fe_2O_3 was observed.

The formation enthalpy divided over all atoms ($\Delta\mathrm{H}_{\mathrm{f}}^{\mathrm{X}}$ /N_{atoms}) was found to be -2.182 eV/atom and -2.120 eV/atom for X = $\mathrm{Fe_{Bi}}$ and $\mathrm{Fe_{Ti}}$, respectively. Each of these measures of stability are comparable with the formation enthalpy per atom of pristine BTO (-2.179 eV/atom). However we would like to note, in terms of global energy, $\mathrm{Fe_{Bi}}$ gains about 5 eV per unit cell increasing the overall stability whereas $\mathrm{Fe_{Ti}}$ loses about 5 eV per unit cell decreasing the overall stability. To further narrow the focus, the configurations that are most likely to form within the stability zone had to be determined by calculating the defect formation energies of each Fe doping configuration using points surrounding the single phase region. The defect formation energies as a probability distribution around the single phase stability zone are shown in figure 5.7.

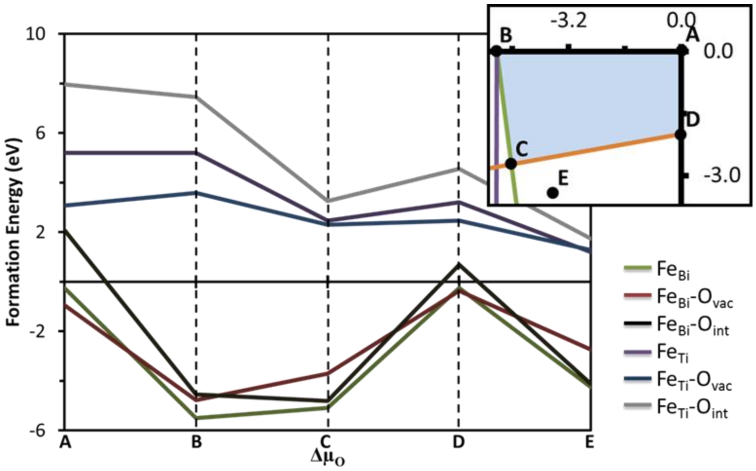

Figure 5.7: Probability distribution of the defect formation energies with respect to the chemical potentials given at points A-E of the chemical potential landscape (shown in the inset). Segment A to B (A to D) represents holding μ_{Ti} (μ_{Bi}) fixed and allowing μ_{Bi} (μ_{Ti}) decrease to the boundary of the stability zone. Point C is the poorest cation condition for both cations and simultaneously the richest μ_O allowed by the stability zone. Point E represents a set of chemical potentials that are associated with DIP formation.

Due to the highly localized nature of the doping, as described in the following electronic structure discussions, it is unlikely that Fe doping configurations would interact significantly with each other unless they are within the first nearest neighbor distance. Hence, the formation energy lines represent probable scenarios in which defect formation is not necessarily a function of defect-defect interaction but primarily a function of the given $\Delta\mu_O$. In the O-poor condition Fe_{Bi} and the composite defect, Fe_{Bi}-O_{vac}, both have favorable probabilities of forming. The second order configuration has greater stability of the two which suggests Fe_{Bi} is likely to always accompany an O_{vac} at this condition. In an experimental study of the off-stoichiometry effects of $BiFeO_3$ (BFO) thin films, in conditions of excess Bi, the XRD patterns only showed reflections corresponding to pure BFO [123], which suggests Fe sits well on a Bi cation sublattice. The implication of our result concurs if we relate the condition of excess Bi to our O poor condition. Formally Fe^{3+} ions have 3d orbitals that are exactly half filled in BFO and Fe_{Bi}. Therefore compatibility emerges between the bonding symmetry of 6s and 3d bonding within the Bi-O' network. For Fe_{Ti} related doping, one can see from their associated formation energies, that they could never form within the confines of the stability zone. This can be explained by Fe ion preference of a 3+ charge state. A Fe^{3+} ion at a Ti^{4+} site is an increase in electron density, therefore the inversion symmetry reduction is reflected as a stability reduction. In terms of photoconduction, this may be related to a charge trapping polaron. The greater stability of Fe_{Bi} in the O rich condition further suggests this notion even in the presence of many energetic O atoms.

From our previous modeling we determined that Fe_{Ti} related doping is unstable, therefore only the electronic structures of Fe_{Bi} related doping will be discussed. Fe_{Bi} related electronic structures should elucidate the electronic signatures that are favorable for increasing photocurrent. The atomic radii for Bi and Fe are 1.60 and 1.40 Å and the covalent radii are 1.46 and 1.25 Å, respectively. Therefore suspecting Fe to create local distortions on the A-cation sublattice is reasonable. The Bi site is formally coordinated with six O atoms and two O' atoms.

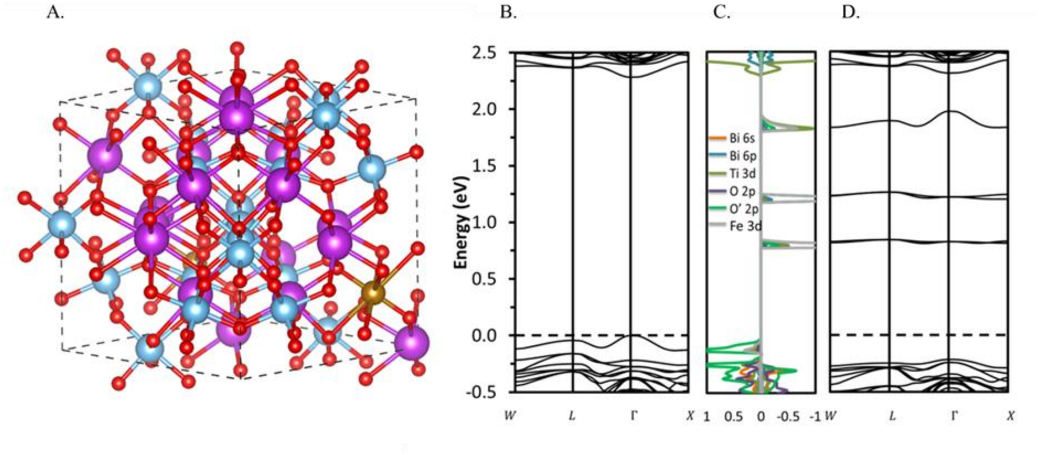

Figure 5.8 A) is the GGA optimized supercell of Fe_{Bi} (In the color diagram: the purple indicate Bi atoms, the cyan Ti atoms, the red O atoms, and brown Fe atom defect), B) is the majority spin channel band structure, C) is the spin polarized PDOS, and D) is the minority spin channel band structure.

In figure 5.8 the GGA optimized unit cell and spin polarized electronic structure for Fe_{Bi} is shown. The six O atoms and two O' atoms surrounding the Fe atom (shown in Figure 7A) have bond lengths of 2.598 and 1.813 Å respectively. This equates to a slight expansion compared to the optimized Bi–O bond length of 2.572 Å and a considerable compression compared to the optimized Bi-O' bond length of 2.236 Å, respectively. By inspection of the bonds along the Bi-O'-Bi chain, distortions associated with the Fe center seem to be compensated by Bi off-centering; the Bi-O' bonds combined range between 2.230 to 2.323 Å. The TiO_6 octahedra associated with this configuration show a preferential elongation of the Ti-O bonds (2.029 Å) along <111> directions. Despite these distortions, balance between the two bonding networks was such that the lattice parameters were a = b = c = 10.327 Å and α = 89.948˚, β = γ = 90.053 ˚. Therefore the global cubic symmetry of the pyrochlore structure is retained just as it is predicted by the stability zone analysis of the formation energies. In figure 5.8 B), the majority spin channel band structure of Fe_{Bi} is shown. Mid gap states are absent and the band gap is direct at the Γ-point with a value of 2.282 eV. This is a significant band gap reduction from the calculated band gap of pristine BTO (2.556 eV). In figure 5.8 C), the site projected density of states (PDOS) shows that the VBM has predominantly O' 2p character, and the lowest conduction band states are Ti 3d-like. This feature is favorable for photocurrent because it is a highly rate electronic transition, according to selection rules. From figure 5.8 D), it can be seen in the minority spin channel band structure that there resides five unoccupied mid gap bands. The shapes of the mid gap bands suggest they were formally the five upmost valence bands of the majority channel. Of these unoccupied bands, the four with the lowest energy, overlap in pairs at approximately 0.75 and 1.25 eV above the Fermi level. Both groupings show their strongest degeneracy at the Γ-point which may be related to anisotropic ordering of the spins. In a theoretical study of BFO crystals, DFT calculations correctly reproduced experimentally-observed ordering of magnetic polarization along <111> directions of a cubic perovskite-like lattice [124]. The authors characterized this ordering as ferroelectric and concluded that it essentially originated from displacement of Bi atoms relative to the center of FeO_6 octahedra.

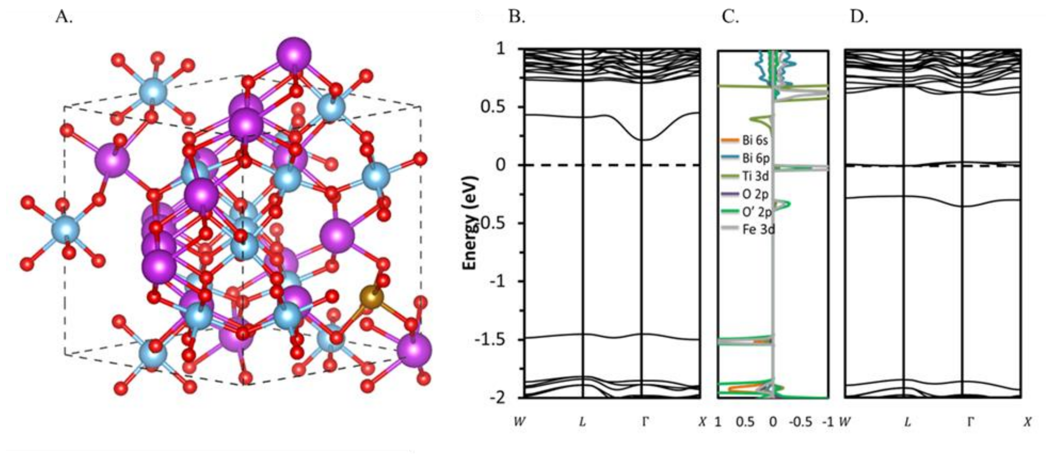

Figure 5.9: A) is the GGA optimized supercell of Fe_{Bi}-O_{vac}, B) is the majority spin channel band structure, C) is the spin polarized PDOS, and D) is the minority spin channel band structure.

Figure 5.9 shows the GGA optimized supercell and spin polarized electronic structure for Fe_{Bi}-O_{vac}. The relaxed lattice parameters of figure 5.9 A) were a = b = c = 10.316 Å with α = 89.892˚ and β = γ = 90.108˚, which resulted in a unit cell volume of 1097.915 Å^3. This reflects a volume decrease from the pristine BTO (1102.922 Å^3). Yet, the local bonding changed such that the cubic symmetry was maintained. The Fe atom is coordinated with three O atoms and one O' atom to form a planar pyramid. The Fe-O' distance, opposite to the void created by the O'$_{vac}$, composes the tip of the planar pyramid. Compared to the optimized Bi-O' distance of 2.236 Å, the Fe-O' distance is a considerable contraction at 1.971 Å. The three corner-shared O atoms, form the base, and are all 2.224 Å away from the Fe center. This is a significant compression as compared to the optimized Bi-O bond length 2.572 Å. The TiO_6 octahedral units are uniformly distorted with preferential elongation of the Ti-O bonds (2.083 Å) along a <111> direction as they are in the Fe_{Bi} case.

In figure 5.9 B), the majority spin channel band structure shows that there are two isolated bands one occupied and one unoccupied roughly 0.3 eV from their respective band edges. The curvature of the bands and respective intensities of the PDOS, shown in figure 5.9 C), indicate that both the VBM and the occupied mid gap band have considerable O' 2p character however they differ by the predominant cation contribution. In the VBM Bi 6s has intensity at least three times that of Fe 3d, whereas for the occupied mid gap band Fe 3d has a stronger intensity than Bi 6s. The CBM and the unoccupied mid gap band are both Ti 3d-like, however the unoccupied mid gap band has deep curvature at the Γ point indicating a reduced charge carrier mass along the <111> and <110> conduction pathways. In a previous theoretical work [75], α-Fe_2O_3 doped with Ti experienced the greatest enhancement of photocurrent due to increased polaron hopping probabilities related to a net compression of the unit cell. The authors concluded that some combinations of substitutional 3d transition metals act as electron donors and reduce the effective mass for electrons. Our Fe_{Bi}-O_{vac} cell shows the same characteristics but in relation to s-p substitution instead of d-d. In general, increased polaron hopping would increase solar-to-hydrogen conversion by facilitating the separation and transport of photo-generated charge carriers. Figure 5.9 D) shows that the minority spin channel band structure has two mid-gap states, both occupied with an energy difference of 0.185 eV, centered at the L-point. However, the energy difference between the VBM and the lowest energy occupied mid gap band is around 1.5 eV measured at the Γ-point. The energy difference between the CBM and the uppermost occupied mid gap band is roughly 0.75 eV, also measured at the Γ-point. The composition of the mid gap bands shows some disparity between the cation contributions similar to the previous Fe_{Bi} case, but the relative intensities are merely fractions by comparison.

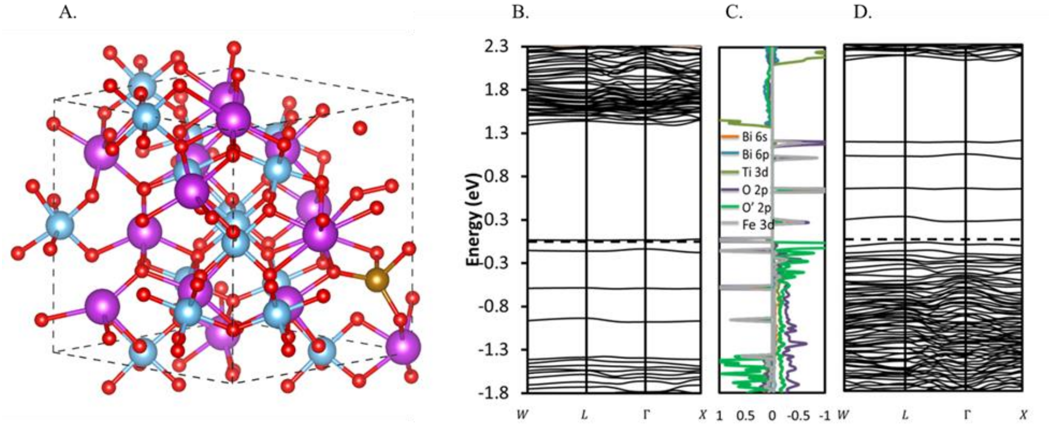

Figure 5.10: A) is the GGA optimized supercell of $\mathrm{Fe_{Bi}}$-$\mathrm{O_{int}}$, B) is the majority spin channel band structure, C) is the spin polarized PDOS, and D) is the minority spin channel band structure.

Figure 5.10 shows the GGA optimized supercell and spin polarized electronic structure for $\mathrm{Fe_{Bi}}$-$\mathrm{O_{int}}$. The relaxed lattice parameters of $\mathrm{Fe_{Bi}}$-$\mathrm{O_{int}}$ were a = 10.425 Å, b = 10.409 Å, c = 10.371 Å with α = 89.258˚, β = 90.070˚, and γ = 89.596˚, which results in a unit cell volume of 1125.282 $Å^3$. This is a considerable expansion from the pristine BTO unit cell volume. Note that the cell angles and lattice parameters trend toward non-cubic symmetry in the $\mathrm{Fe_{Bi}}$-$\mathrm{O_{int}}$ case. At this point it is also worth mentioning that this configuration is at the stability zone boundary with the richest O condition, so it can be considered as representing the point at which $\mathrm{Fe_{Bi}}$ related doping should experience a phase transition or likely coexistence of a DIP. The Fe atom is coordinated with two O atoms and two O' atoms as shown in figure 5.10 A). Similar to the previous case the Fe atom is centered in a distorted planar pyramid. The difference is that it shares one of its edges (the one between O and O' atoms) with a Bi centered octahedral. The interstitial which started as a nearest neighbor of the Fe atom ended up 3.863 Å away from the Fe atom. It shares a corner with the Bi centered octahedral and composes an edge of a $\mathrm{TiO_7}$

unit. The O_{int}-O bond length is 1.461 Å. The TiO_6 octahedrons have one bond randomly elongated in either a <111> or <110> of 2.112 and 2.034 Å, respectively.

The most noticeable electronic features for Fe_{Bi}-O_{int} are four non-dispersive mid gap bands between the majority and minority spin channel band structures as shown in Figures 5.10 B) and 5.10 D) respectively. In the majority spin channel these mid gap bands are occupied. The most energetic of them is at the Fermi level 1.362 and 1.339 eV from the VBM and CBM respectively (centered at the Γ- point). This feature can be related to Fermi level pinning. The three bands lower in energy are approximately 0.4 eV apart with the upper most of these three around 0.1 eV below the Fermi level. Figure 5.10 D) shows that in the minority channel the mid gap states are all unoccupied but have a similar shape and spacing as they had occupied in the majority channel. The upper most mid gap band is 0.946 eV from the CBM and the lowest unoccupied mid gap band is 0.296 eV from the VBM. The PDOS, Figure 5.10 C), shows that the mid gap bands are primarily Fe 3d states in both spin channels suggesting massive charge carriers and high probability of exciton recombination. In an experimental study of $Bi_4Ti_3O_{12}$ thin films, a decrease in the electrical properties for films grown at an oxygen partial pressure exceeding 200mTorr was reported [125]. The authors concluded that oxygen interstitial ions were responsible for a reduction in the Schottky barrier height between the electrode and thin film. The nature of a Schottky barrier with insufficient height is based on two facts (i) interfacial mismatch between two different phases and (ii) an increase of space charge limited currents. Therefore this configuration has an electronic signature indicative of a coexistent DIP and reduced photocurrent, ultimately excluding it from the set of single phase allowed Fe doping configurations.

Chapter 6

Charge Transport

6.1 Introduction

Bi- and Ti-based metal oxides are routinely looked upon to be the functional component in various applications of solar energy conversion due to their light activated charge transport. For example, TiO_2 has the reputation for being a water splitting photocatalyst because of its ability to facilitate redox reactions between photogenerated charge carriers and water molecules [15,126–129]. The major feature of TiO_2 is that its band gap straddles the redox potentials of water which makes it catalytic in that environment when irradiated by sunlight. Unfortunately, harnessing the solar energy is plagued with limited range spectral absorption. The bandgap of TiO_2 is too large for it to effectively split the water molecule into both hydrogen and oxygen gas. In practice, only hydrogen evolution is ever measured [108,127,130,131], which has low rates, and the required energy to drive the reaction is in the ultraviolet range. Therefore, a plethora of band engineered titania based materials have been developed over the years as attempts to obtain narrower band gaps [13,14,16,132–136]. In particular, the pyrochlore bismuth titanate, $Bi_2Ti_2O_7$ (BTO), a compound best described as an alloy of TiO_2 and Bi_2O_3, has many unique structural and electronic properties that can be fine-tuned to more efficiently split the water molecule [36,44,52,52,53,85,137–139]. Based on its optical band gap (2.88 eV), band edge alignments, low cost, terrestrial abundance, low toxicity, and defect accommodating pyrochlore structure, it is certainly an ideal candidate for photocatalytic performance optimization.

Pyrochlore BTO has cubic symmetry belonging to the Fd3M space group (#227). In addition to its two different cation sub-lattices, BTO has to different types of oxygen atom, O and O’, which are differentiated by their coordination with Bi atoms. O atoms are shared by both cations where O’ atoms are bonded with Bi atoms only. In figure 6.1 we show the GGA-DFT calculated electronic structure and spectral absorption curve of BTO. BTO possess enhanced performance compared to TiO_2 on account of its broader ranged spectral absorbance. Our simulated spectral absorbance, Figure 6.1 A), shows significant area under the absorption curve from 400 to about 600 nm, which is a considerable portion of the visible range of light. It can be seen in Figure 6.1B, that the valence band maximum (VBM) and conduction band minimum (CBM) show nice dispersion at the Γ point as well. From the projected density of states, shown in Figure 6.1C, the presence of Bi 6s lone pairs at the VBM effectively reduce the band gap compared to TiO_2 and the presence of Bi 6p states in the conduction band effectively reduced negative charge carrier masses.

Interestingly, we found BTO to have a propensity for modification by band engineering techniques for a narrow selection of allowable transition metal dopants. These allowable transition metal dopants generally facilitate band gap reduction in a near linear fashion with dopant concentration. Also, the favorable electronic transition, O 2p - Ti 3d, is typically maintained without too many dopant related states being mixed in. In another study we found formation of dopant inspired phases (DIPs) to be detrimental to BTO photoconduction, but also, with careful consideration of the growth conditions, they can be avoided [140]. The range of chemical potentials inherent to different synthesis methods, are straight forward thermodynamic relationships. However, irrespective to the quality of pure phase doping or the reproducibility of increased spectral absorbance, repeatable enhanced photocurrent still evades.

The band gap range for photocatalytic water splitting is 1.23 – 3.0 eV [141], thus a low absorption coefficient is not the primary factor for BTO, nor are the band edge alignments or any other band conduction properties. The primary factors are charge recombination, charge trapping, and charge diffusion, which are more related to polaron hopping. Other than maximization of BTO's aspect ratio for optimal solar absorption and subsequent charge diffusion, how else does one prescribe enhancing the conduction properties? In this paper, we use ab initio quantum mechanics to gain insight from the atomic level as to how doping BTO with allowable transition metals (Cr, Mn, Fe) will affect its charge transport. Since the transport properties of BTO have not been explored theoretically before, we have used a plane wave code to determine its transport properties using the small polaron model.

We follow the conventional GGA + U approach to compensate for the overestimation of electronic delocalization for our plane wave calculations. Our goal was to determine the conduction parameters of BTO but also make additional evaluations in regards to the validity and procedural aspects of DFT transport modeling. Furthermore, finding a measured activation energy for transport in BTO has been difficult. As such we rely on calibrating our model by reproducing some of the more prevalent results found in the literature for TiO_2 and $BiVO_4$. We aim to conduct an electron transport model of BTO and doped-BTO to increase our understanding of the transport mechanisms.

6.2 The Small Polaron Model

The small polaron model used here is akin to the Marcus two-state model [142,143] and other developments like those done by Emin and Holstein [144–148] and Austin and Mott [149] whereby an electron 'hops' from site to site in relation to a movement of nuclear positions. Polaron hopping between two adjacent Ti atoms ($\mathrm{Ti_A}$ and $\mathrm{Ti_B}$) in relation to an antiphase vibrational mode of a crystal lattice is depicted as three relevant states in Figure 6.1.

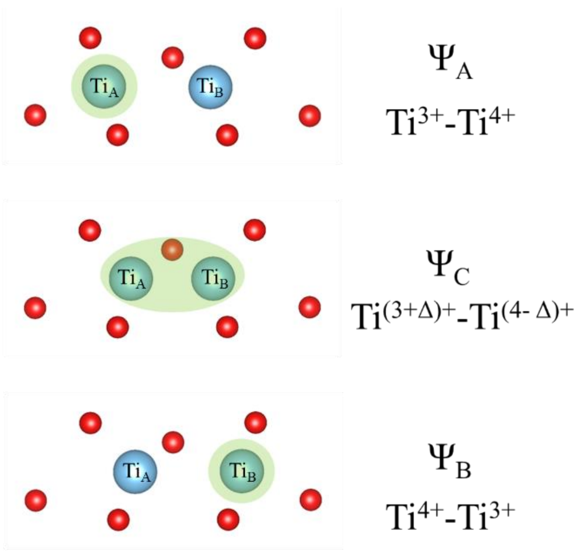

Figure 6.1: Schematic depiction of the three relevant states of electron transfer with respect to an antiphase movement of nuclei. Ψ_A is the initial state where excess charge is localized on the right cation. Ψ_B is the final state where excess charge is localized on the left cation. Ψ_C is the intermediate transition state where a likely dipole transition occurs as a mechanism to drive the polaron movement.

The initial state, Ψ_A represents a negative polaron localized on the left cation which has an electronic configuration of $\mathrm{Ti(III)} - \mathrm{Ti(IV)}$. As the right cation gets closer to the bridging O atom its configuration becomes increasingly polar with its dipole axis along the conduction pathway. The transition state, Ψ_C represents the movement of the negative polaron from the left to the right cation, which at the optimal reaction coordinate has an electronic configuration of $\mathrm{Ti(III} + \Delta_\mathrm{L}) - \mathrm{Ti(IV} - \Delta_\mathrm{R})$ and $(\mathrm{III} + \Delta_\mathrm{L}) = (\mathrm{IV} - \Delta_\mathrm{R})$. An important aspect shown in Figure 6.1 is the position of the bridging O atom in relation to the localization of the polaron. A longer bond is shown between the reduced Ti atom and the O atom as it is commonly observed. Only at the transition state does the cation-anion bond lengths of $\mathrm{Ti_A}$-O and O-$\mathrm{Ti_B}$ become the same. The next instant, the final state, Ψ_B

represents the negative polaron localized on the right cation which has an electronic configuration of $\mathrm{Ti(IV)} - \mathrm{Ti(III)}$. Of course the following instant $\mathrm{Ti_A}$ returns to $\mathrm{q_A}$ and the process moves along to the right. This is our basis for simulating the nuclear movements associated with small polaron hopping in a crystal lattice.

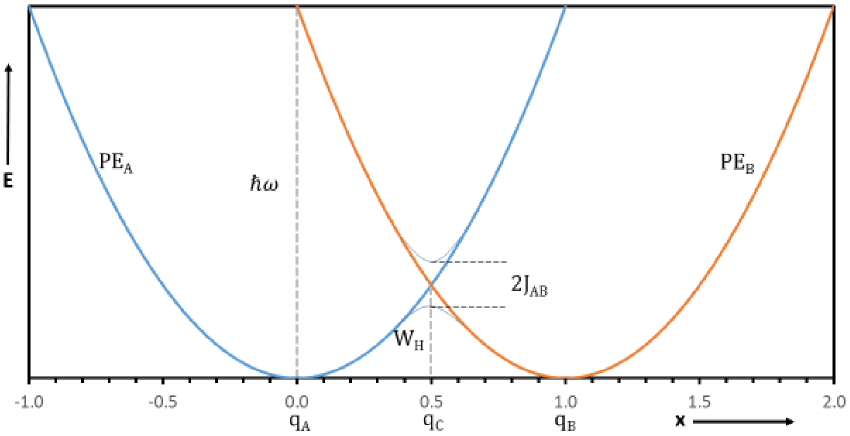

Figure 6.2: General features of the small polaron model. The potential energy surfaces $\mathrm{PE_A}$ and $\mathrm{PE_B}$ are of the initial and final states respectively, which are assumed to be parabolic with their minima centered on the equilibrium configurations $\mathrm{q_A}$ and $\mathrm{q_B}$. $\mathrm{q_C}$ is the transition state where the initial and final states have their greatest interaction. The energy of the final state at the $\mathrm{q_A}$ configuration is labeled $\hbar\omega$ as this energy can be overcome by photon assistance. The diabatic activation energy is shown as $\mathrm{W_H}$. The adiabatic energy curves are shown as dashed lines with the electronic coupling matrix element $\mathrm{J_{AB}}$ given as twice the energy difference between the two adiabatic states.

The electron transfer parameters with respect to a cross section of the energy profile have been fitted with a linear mathematical model shown in Figure 6.2. The nuclear arrangement of Ψ_A is labeled $\mathrm{q_A}$ and its potential energy curve ($\mathrm{PE_A}$), assumed to be parabolic, is about its center. Likewise, the nuclear arrangement of Ψ_B is labeled $\mathrm{q_B}$

and has its parabolic potential energy curve centered on it ($\mathrm{PE_B}$). The nuclear arrangement of Ψ_C, denoted q_C, is at the crossing point of $\mathrm{PE_A}$ and $\mathrm{PE_B}$ and corresponds to a configuration where the interatomic distance between the cations is reduced by 50%. Three important parameters associated with electron transfer are shown in 6.2 as well; the absorbed photon energy $\hbar\omega$, the nonadiabatic activation energy, W_H, and the electronic coupling element J_{AB} (using the notation of Austin and Mott).

Since the transfer of charge is accompanied with nuclear rearrangements, the polarons formation energy can be considered composed of the electronic energy strain E_e and the lattice energy strain E_l e.g. $\Delta H_f^{pol} = E_e + E_l$. J' represents the band with between the initial and final states. W_D, not shown in 6.2, is the activation energy due to disorder. For a more detailed discussion about the definitions and relationships thereof the reader is directed to the review paper by Austin and Mott.

Our focus is on trends in the activation energy, since the mobility of carriers depends exponentially on its value

$$\mu \propto e^{-W_H/kT} \tag{6.1}$$

Where μ is the electron mobility, T is the temperature, and k is the Boltzman constant. The electron conductivity can be calculated from the electron mobility using the equation

$$\sigma = en\mu \tag{6.2}$$

Where σ is the electron conductivity, e is the electron charge, and n is the electron carrier concentration.

6.3 Computational Details

Periodic calculations were used to determine the equilibrium configurations q_A and q_B of the charge neutral structures. These calculations were performed using the

Vienna ab initio Simulation Package (VASP 5.2.2) [37–39,150] which utilized the projector augmented-wave method and a plane wave basis set (E_{cut} = 600 eV) to describe the interaction between core and valence electrons. Representation of the electronic exchange and correlation energies was handled by the Perdew-Burke-Ernzerhof (PBE) GGA exchange-correlation (XC) functional [25]. The starting coordinates for TiO_2 and BTO structures were defined by their respective cells that have 48 and 88 total atoms respectively, and are shown in figure 6.3.

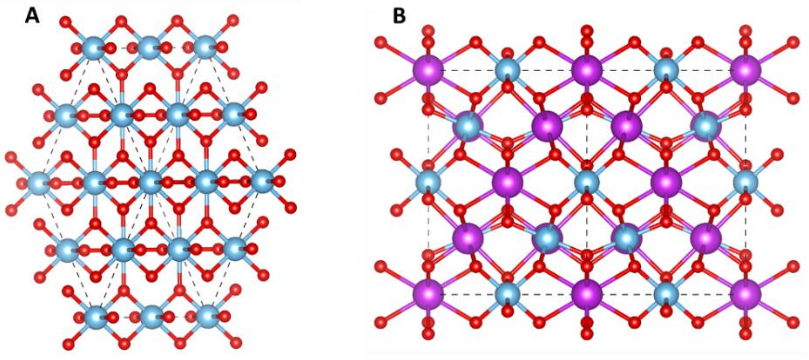

Figure 6.3: A) is the relaxed 2X2X1 super cell of rutile TiO_2 shown in the [111] perspective and B) is the relaxed unit cell of BTO shown in the [101] perspective. Ti atoms in each structure are represented by cyan colored spheres, O atoms by red spheres and in B) Bi by purple spheres.

Full optimization of these structures was based on relaxation of the electron and ion positions as well as the overall cell volumes until the residual forces between atoms became lower than 0.01 eV/Å. The simulation parameters were well converged for Monkhorst pack k-point meshes (3 X 3 X 6 for rutile TiO_2 and 3 X 3 X 3 for BTO variations) where the partial occupancies were set by the tetrahedron method with Blöchl corrections. Our calculations gave lattice parameters of a = 4.605 and c = 2.972 Å for rutile TiO_2 and 10.329 Å for the cubic pyrochlore BTO which agrees well with other theoretical and experimental studies. The shortest Ti-Ti interatomic distance for TiO_2 was found in the [111] direction at 3.579 Å and for BTO in the [101] direction at 3.652 Å. As shown in figure X both structures have the axes of bridging O atoms perpendicular to their conduction paths.

As the DFT functional is known for its electronic correlation effects and lack of derivative discontinuities that lead to an erroneous representation of calculated electronic structures with d and f orbitals, a strategy for compensating these shortcomings had to be used. In particular the self-interaction of unpaired electrons produces a delocalized description of excess charge, which greatly affects proper modeling of small polarons in DFT. Several approaches to correcting electron self-interaction have been proposed. Of these, the most popular approaches are hybrid-DFT, an ad hoc mixing of the exact Hartree-Fock exchange, or DFT+U, inclusion of extra electron correlation. We chose DFT+U, as it produces electronic properties that are comparable to those from hybrid-DFT while being computationally benign. Instead of adding exchange energy to the Kohn-Sham particles it provides extra correlation via a corrective Kohn-Sham self-interaction operator. The specific type of DFT+U followed the simplified rotationally invariant form proposed by Dudarev and others [35] whereby the on-site Coulomb term U and the exchange term J are grouped as a single effective parameter (U-J), we refer to it as U_{eff} throughout this paper.

Our application of the polaron hopping theory within the framework of DFT began with determining the change in total energy as Ti_A and Ti_B are moved along their potential energy surfaces. We used a linear interpolation method to determine the change in coordinates for Ti_A and Ti_B separately. As depicted in Figure 6.2, localization occurs on the Ti atom that does not experience the coordinate change. Thus changing the coordinates of Ti_A causes the excess charge to localize on Ti_B.

$$\vec{q}_x = (1 - x)\vec{q}_A + (x)\vec{q}_B \tag{6.3}$$

In Equation 6.3 we show the linear combination of vectors q_A and q_B used to determine the path for Ti_A, the path for Ti_B was obtained by exchanging the variable dependent factors in parenthesis. The variable x ranged from 0 to 1 in each case and corresponded to a fraction of the relaxed interatomic distance between Ti_A and Ti_B. With these points we determined the potential energy curves individually, to simulate an antiphase vibrionic motion of the cations. The PE curves are classified as adiabatic because the hopping in BTO is expected to occur upon thermal excitation, which is manifested here by our simulation of antiphase vibration.

6.4 Negative Small Polaron in TiO_2

In GGA + U calculations it is necessary to determine an appropriate U_{eff} value to handle corrections for the self-interaction effect. As there is no universal value of U_{eff} that works equally well for all materials or for all properties of interest it is logical to choose a U_{eff} value that is a compromise between the reproducibility of geometric and electronic structures and the properties of interest. For rutile TiO_2 many examples are provided in literature where the compromise was made with respect to the experimental band gap (3.0 eV) and lattice parameters (a = 4.593 and c = 2.958 Å). For instance, in a theoretical study on defect states on the rutile TiO_2 surface, the authors carefully analyzed localization of a gap state with respect to their implementation of “Dudarev U” and found one that exactly matched experiment when U_{eff} = 4.20 eV [151]. At this value their quoted lattice parameters were a = 4.669 and c = 2.970 Å and their band gap was 2.68 eV. On the other hand, in GGA+U study on polaron hopping in TiO_2, the authors concluded that a U_{eff} = 10 eV the crossing point energies for polarons saturated around

0.3 eV for anatase TiO_2 [152]. At this value of U_{eff} they quoted lattice parameters of a = 4.65 and c = 2.97 Å, and a band gap of 3.04 eV.

In figure 6.4 we show a plot of the crossing point energies for TiO_2 as a function of U_{eff} within our model. Similar to ref 124, we obtained a saturation of the activation energies but for rutile TiO_2, that were around 0.315 eV. In rutile TiO_2 the effect of on-site Coulomb potential tends to reduce the overlap between Ti 3d orbitals and O 2p until no additional change in the localization of the 3d electrons occurs.

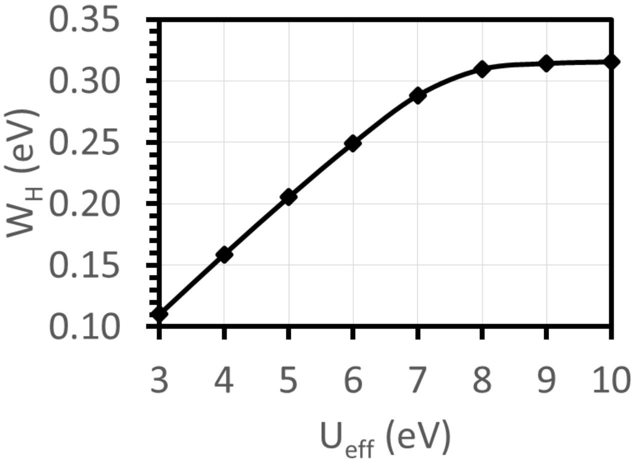

Figure 6.4 Crossing point energies as a function of U_{eff}. Saturation of the crossing point energies occurs around U_{eff} = 8 eV.

With our method benchmarked we determined the PE surfaces for Ti cations in rutile TiO_2. In figure 6.5 we show the cross section of the energy profile for negative small polaron transport in rutile TiO_2.

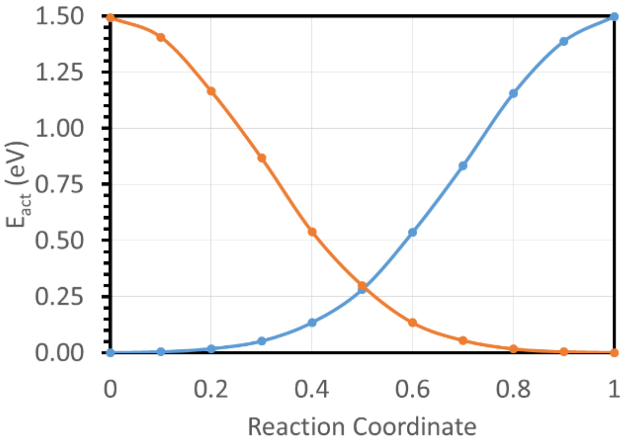

Figure 6.5 Cross-section of the energy profile of negative small polaron transport in rutile TiO_2. Both curves are near parabolic indicating the small polaron model is adequate to describe electron transfer in this system.

According to figure 6.5, the diabatic polaron activation energy, W_H, is 291 meV and the lattice reorganization energy, ħω, is 1.493 eV. In comparison to reference 124 the activation energy is nearly equivalent, but the reorganization energy is slightly high. This is likely due to a combination of DFT's self-interaction error, the high energy plane wave cut-off value, and the use of an unphysically high effect u parameter (U_{eff} = 10 eV) in the implementation of DFT+U. Given the faults of DFT transport modeling we consider the results to be authentic.

6.5 Positive Small Polarons in $BiVO_4$

We used our method to determine positive small polarons in BVO to further benchmark our method. In figure 6.6 we provide the cross-section of the energy profile of positive small polaron transport in BVO. It shows W_H to be around 250 meV and ħω to be around 400 meV. This result is interesting because for the theoretical purpose we did not employ any effective U parameter (U_{eff} = 0 eV). Others have calculated activation energies for BVO to be around 80 meV using the hybrid density functional theory approach(PBE-HF25%) [153]. The increase exchange energy with respect to our calculation actually resulted in a lower activation energy. As the semi-localization of excess charge is spread over a larger distance, the activation energy obtained is of a different species, perhaps a positive large polaron instead.

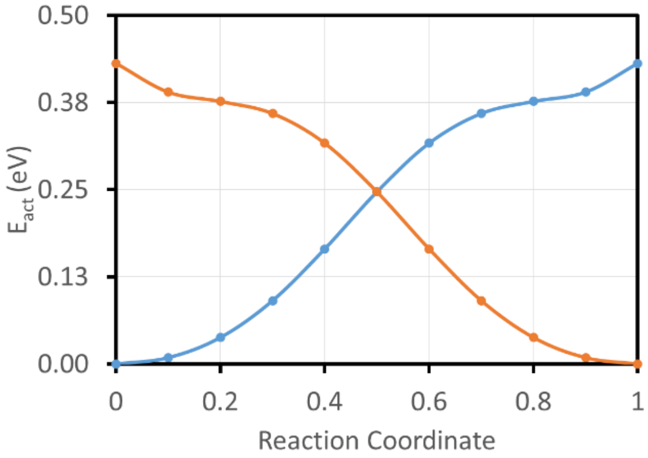

Figure 6.6 Cross-section of the energy profile for positive small polaron hopping in BVO. For the theoretical purpose $U_{eff} = 0$.

It is a well establish fact that treatment of the self-interaction errors are necessary to properly model polaron transport using DFT. However in an experimental study on the combined charge carrier transport of $BiVO_4$ the authors report activation energies of 286 meV and 290 meV for Mo and W doped BVO respectively [154]. A value for reorganization energy is not reported. In another theoretical study for polaron hopping in BVO, the authors state the polaron activation energy increases monotonically with increase percentage HF exchange [155]. They report the activation energy to increase from 100 meV to 460 meV with α 5% to 25%.

6.6 Negative Small Polarons in BTO

From our polaron modeling for the multi metal oxide BVO we considered systematically determining an effective U parameter for our prototype BTO. From preliminary calculations of the band gap and electronic structure of BTO effective U on Ti 3d orbitals had negligible effect on the electronic properties. In figure 6.7 we show a plot of the activation energy as a function of effective U parameter.

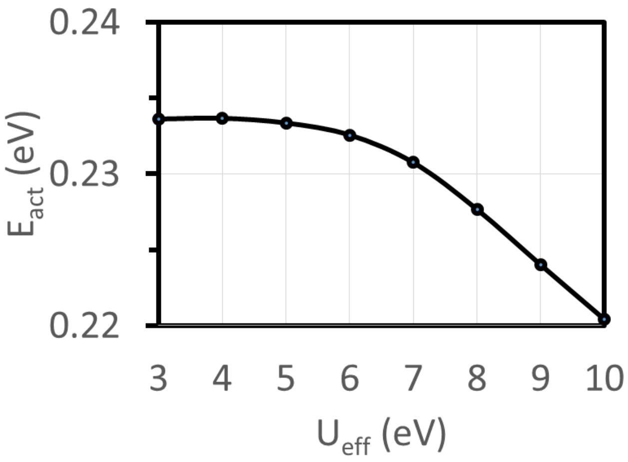

Figure 6.7 Polaron activation energy as a function of effective U parameter for pristine BTO.

From figure 6.7 it can be seen that there are small changes with increased U parameter for negative small polaron transport in BTO. It can be seen that activation energy is its lowest at U_{eff} = 10 eV. From our results we have determined that for a mixed metal oxide that has a defect accommodating crystal structure such as BTO, low U_{eff} values can be used to obtain reasonable results. For the remaining polaron discussions we use U_{eff} = 3 eV.

6.6.1 Polarons in Pristine BTO

In figure 6.8 we show a cross-section of the energy profile for negative small polarons in pristine BTO. The activation energy W_H is shown to be 233 meV which corresponds to improved photoactivity over TiO_2. The reorganization energy is shown to be 1.235 eV.

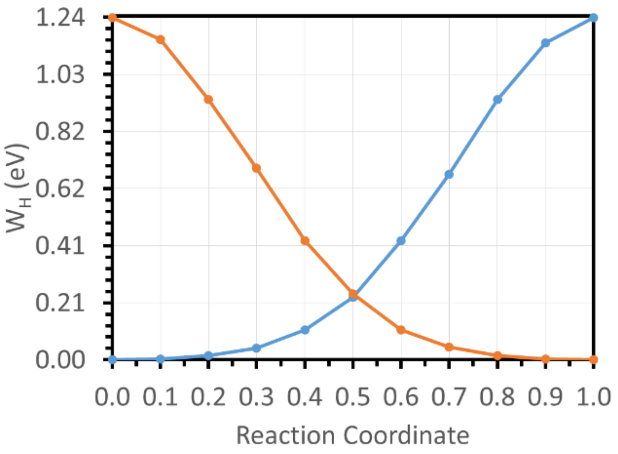

Figure 6.8 Cross-section of the energy profile of negative small polaron transport in BTO.

Our results for BTO are reasonable in comparison to our benchmarked results for TiO_2. It is known that BTO has a higher photoactivity, thus the lower polaron activation energy correlates. Also the lower reorganization energy corresponds to the extra degree of freedom afforded to BTO by its Bi-O’-Bi chains which undergo cation off-centering as a mechanism to retain its cubic structure.

Bader analysis using the code provided by Henkelman et. al. [103,104] was used to analyze the atomic charges as snap-shots of the electron transfer process. In figure 6.9 we show atomic charge as a function of all atoms for movements of Ti_A and Ti_B respectively. Each series is with respect to the configuration variable x, numbers 1-16 refer to Bi atoms, numbers 17-72 refer to O atoms, and numbers 73-88 refer to Ti atoms. From these atomic charge spectra it can be seen that charge oscillates across specific Bi, Ti, and O atoms during the electron transfer process depending on which Ti atom is being moved. The largest peaks, which are common for figures 6 and 7 correspond to atoms 9,14,36,73 and 79. 9 and 14 are Bi atoms that are bonded to the bridging O atom, 36, where 73 and 79 are Ti_A and Ti_B respectively.

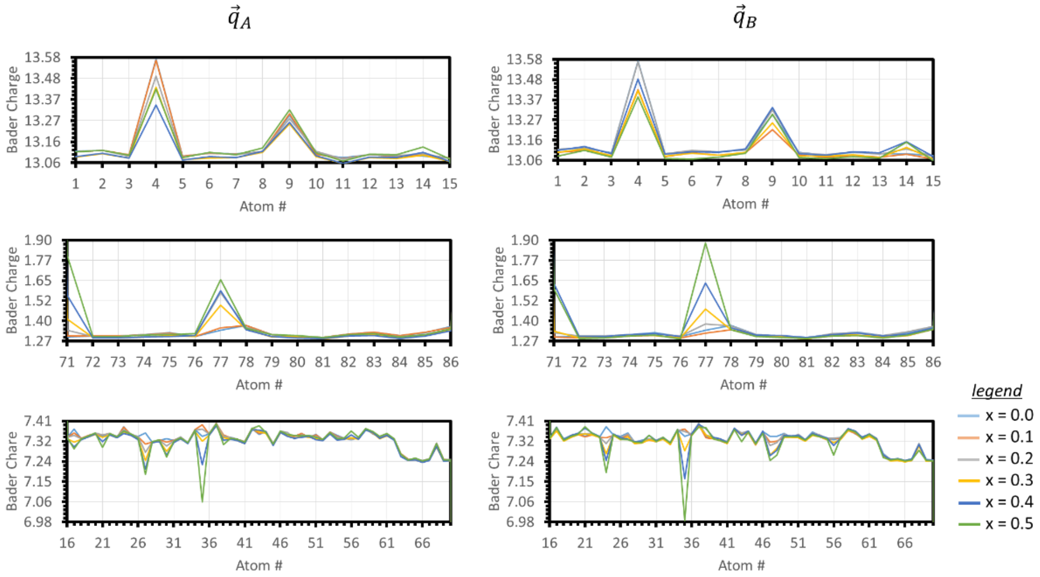

Figure 6.9 Bader analysis plot given as charge vs atom in the BTO lattice. The left column refers to chare localized on Ti_A at q_A and the right column refers to charge localized on Ti_B at q_B. In the legend, x refers to the reaction coordinate parameter.

In figure 6.9 it is shown for each reaction coordinate that up to three Bi atoms gain charges and many O atoms lose charges even though only Ti atoms are participating in the electron transfer process.

6.6.2 Negative Polarons in TM Doped BTO

To model determine the polaron hopping parameters for transition metal doped BTO we consider the favorable doping configuration found in chapter 5, Cr_{Bi}-O_{vac}, Mn_{Bi}-O_{int}, and Fe_{Bi}. In each case Ti 3d and the transition metal d orbital have extra on-site correlation energy characterized by U_{eff} = 3 eV.

In figure 6.10 cross-sections of the favorable doping configurations in BTO are shown. For Cr_{Bi}-O_{vac} the activation energy and reorganization energy are shown to be 253 meV and 1.422 eV respectively. For Mn_{Bi}-O_{int} the activation energy and reorganization energy are shown to be 254 meV and 1.39 eV respectively. At last, for

Fe_{Bi} the activation energy and reorganization energy are shown to be 207 meV and 1.074 eV respectively.

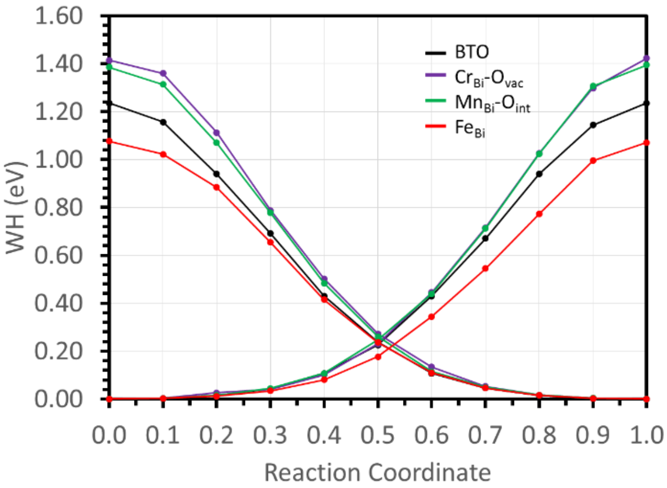

Figure 6.10 Cross-section of the energy profile for negative small polarons in transition metal doped BTO. The black curve represents pristine BTO, the purple curve represents Cr_{Bi}-O_{vac}, the green curve represents Mn_{Bi}-O_{int}, and the red curve represents Fe_{Bi}.

In comparison to pristine BTO, Fe_{Bi} is the only doping configuration that improves polaron transfer in BTO. The activation energy is decrease by 26 meV and the reorganization energy is decreased by 161 meV. This indicates both intrinsic defects are detrimental to electron transfer as they serve as recombination and trapping centers.

Chapter 7

Conclusions

7.1 Stability

We have systematically studied the nature of X = Cr, Mn, and Fe doping in BTO. Evidently, incorporation of these 3d transition metals in BTO increases its visible light absorption. The band gap of BTO was reduced on average by 0.3 eV upon X doping. Substitutions in the A-sites are energetically favored compared to substitutions in the B-sites. Depending on occupation of the 3d levels, O vacancies or interstitials accompany the doping. X_{Ti} related doping configurations in general had positive formation energies with respect to the single phase stability zone. The X_{Ti}-O_{int} doping configuration was the most favorable with respect to Ti-poor/Bi-rich conditions in each case. As these defects are unstable, they can be associated with formations of secondary phases. With respect to the experimental evidence, our results showing Cr_{Bi}-O_{vac} to be the most favored doping configuration, suggested Cr ions have charge states that are predominantly 3+ in BTO, which supports our prediction of Bi-site substitutions being more stable. Mn_{Bi}-O_{int} as a the most favored configuration suggest Mn ions are most likely in a 4+ charge state which would require a coordination change with O atoms in the Bi-site. Fe_{Bi} as the most favored doping configuration in BTO suggested Fe ions are most likely in a 3+ charge state. Ti-poor conditions are associated with formations of secondary phases. The favorable X doping configurations all had some common features which may be responsible for increasing photocurrent. For example, each favorable doping configuration preserved cubic symmetry. The flexibility of O’-Bi-O’ chains were used to compensate local distortions. TiO_6 octahedra remained rigid, by not changing their coordination with O atoms.

7.2 Electronic Structure Doping

The electronic structures of the favorable transition metal doping configurations have distinct features with respect to d electron configuration and the existence of anion defects. Many mid gap states occur that can serve as electron donors but due to the nature of the doping many of the states are flat indicating heavy effective masses. Of the favorable doping configurations those with intrinsic defects had the most negative influence on the electronic band structure. In each case enhanced spectral absorption was achieved but enhance photocurrent was not always reciprocated.

7.3 Polarons

We have shown that polarons hopping in BTO can be modeled using DFT. For multi metal oxides the self-interaction errors are partially addressed by the complexity of multiple cations. For BTO the effective U parameter was adequate at 3 eV. We found among the favorable doping configurations that Fe_{Bi} has the overall most positive influence on enhancing the photocatalytic performance of BTO. Fe-BTO polarons have activation energies 26 meV less than pristine BTO. Ultimately, the validity of using DFT to model polaron transport hinges on the correct application and intuitive combinations of increased exchange and correlation energies.

Chapter 8

Future Directions

Almost every multi metal oxide photocatalyst has an optimal dopant concentration beyond which functional enhancements decline. It is an aim to extend our methods to go beyond this barrier. Therefore work on obtaining a mechanism to induce phase stabilities of complex materials with higher and higher concentrations of dopant is paramount. Also, the study of solar conversion materials should include surface studies of complex materials. For instance, the photoelectrochemical process occurs on the surfaces of photocatalytic materials. On the surface magnetic coordination dictates the adsorption properties and is the primary mechanism for interfacial optimization. Therefore we anticipate further study of the surface magnetic effects on the performance of semiconductors in general.

In the field of material design, structure predicting algorithms are among the hottest topics. With the fact functional materials are becoming more and more complex, standardized interactions fail to predict the equilibrium structures. Therefore it is an aim to investigate new methods for developing structure prediction tools. As computers become faster and cheaper high data throughput methods are of interest. Work is needed on building databases to support the random access memory of learning machines in computational physics and chemistry. It is a goal to automate discovery in science and technology where artificial intelligence is used to accelerate the advancement of mankind.

Finally, more fundamental aspects of quantum mechanics have become emergent topics such as quantum decoherence. For example, increasing optical absorptions also increase optical emissions. Therefore decoherence is needed to decouple these responses to obtain advanced efficiency functional materials. Quantum entanglement or the so-called ‘spooky action at a distance’, is an interesting topic in general, but even more intriguing is its many potential applications in conjunction with functional materials.

References

[1] B. I. Cook, J. E. Smerdon, R. Seager, and S. Coats, Clim. Dyn. **43**, 2607 (2014).

[2] M. L. Roderick, F. Sun, W. H. Lim, and G. D. Farquhar, Hydrol. Earth Syst. Sci. **18**, 1575 (2014).

[3] W. J. Sydeman, M. García-Reyes, D. S. Schoeman, R. R. Rykaczewski, S. A. Thompson, B. A. Black, and S. J. Bograd, Science (80-.). **345**, 77 (2014).

[4] F. Courchamp, B. D. Hoffmann, J. C. Russell, C. Leclerc, and C. Bellard, Trends Ecol. Evol. **29**, 127 (2014).

[5] J. T. Houghton, *Global Warming : The Complete Briefing* (Cambridge University Press, Cambridge, 2009).

[6] G. a Meehl, Science (80-.). **307**, 1769 (2005).

[7] S. J. Davis, K. Caldeira, and H. D. Matthews, Science (80-.). **243116**, 1330 (2010).

[8] S. S. Chandel, R. Shrivastva, V. Sharma, and P. Ramasamy, Renew. Sustain. Energy Rev. **54**, 866 (2016).

[9] S. J. Teichner, J. Porous Mater. **15**, 311 (2008).

[10] A. Walsh, SPIE Newsroom 4 (2009).

[11] J. Barber, Chem. Soc. Rev. **38**, 185 (2009).

[12] A. FUJISHIMA and K. HONDA, Nature **238**, 37 (1972).

[13] C. a. Castro-López, a. Centeno, and S. a. Giraldo, Catal. Today **157**, 119 (2010).

[14] J. Zhu, Z. Deng, F. Chen, J. Zhang, H. Chen, M. Anpo, J. Huang, and L. Zhang, Appl. Catal. B Environ. **62**, 329 (2006).

[15] Y. Liu, Z. Wang, W. Wang, and W. Huang, J. Catal. **310**, 16 (2014).

[16] G. Williams, B. Seger, and P. V Kamat, ACS Nano **2**, 1487 (2008).

[17] S. Liu, J. Yu, and W. Wang, Phys. Chem. Chem. Phys. **12**, 12308 (2010).

[18] L. B. Kong, S. Li, T. S. Zhang, J. W. Zhai, F. Y. C. Boey, and J. Ma, Prog. Mater. Sci. **55**, 840 (2010).

[19] P. Erhart, A. Klein, D. Åberg, and B. Sadigh, Phys. Rev. B - Condens. Matter Mater. Phys. **90**, 1 (2014).

[20] V. N. Antonov, Adv. Condens. Matter Phys. **40**, 417 (2011).

[21] H. Coy-Diaz, R. Addou, and M. Batzill, J. Phys. Chem. C **117**, 21006 (2013).

[22] C. D. Chandler, C. Roger, and M. J. Hampden-Smith, Chem. Rev. **93**, 1205 (1993).

[23] Y. Wu, Y. Wu, G. Ceder, T. Supervisor, and G. Ceder, (2014).

[24] P. Hohenberg and W. Kohn, Phys. Rev. **155**, (1964).

[25] J. Perdew, K. Burke, and M. Ernzerhof, Phys. Rev. Lett. **77**, 3865 (1996).

[26] K. Capelle, (2002).

[27] Á. Nagy, Phys. Reports-Review Sect. Phys. Lett. **298**, 2 (1998).

[28] M. Levy, Phys. Rev. A **26**, 1200 (1982).

[29] W. Kohn and L. Sham, Phys. Rev. **385**, (1965).

[30] W. Kohn, Rev. Mod. Phys. **71**, 1253 (1999).

[31] D. Langreth and M. Mehl, Phys. Rev. B **28**, 1809 (1983).

[32] J. P. Perdew and W. Yue, Phys. Rev. B **33**, 8800 (1986).

[33] J. P. Perdew and K. Burke, Int. J. Quantum Chem. **57**, 309 (1996).

[34] J. Perdew, K. Burke, and Y. Wang, Phys. Rev. B **54**, 16533 (1996).

[35] S. L. Dudarev, G. A. Botton, S. Y. Savrasov, Z. Szotek, W. M. Temmerman, and A. P. Sutton, Phys. Status Solidi **166**, 429 (1998).

[36] B. Allured, S. DelaCruz, T. Darling, M. N. Huda, and V. (Ravi) Subramanian, Appl. Catal. B Environ. **144**, 261 (2014).

[37] G. Kresse and J. Hafner, Phys. Rev. B **47**, 558 (1993).

[38] G. Kresse and J. Furthmüller, Phys. Rev. B. Condens. Matter **54**, 11169 (1996).

[39] G. Kresse and J. Hafner, Phys. Rev. B **49**, (1994).

[40] B. Hinojosa, J. Nino, and A. Asthagiri, Phys. Rev. B **77**, 104123 (2008).

[41] W. Wei, Y. Dai, and B. Huang, J. Phys. Chem. C **113**, 5658 (2009).

[42] C. Patterson, Phys. Rev. B **82**, 155103 (2010).

[43] A. L. Hector and S. B. Wiggin, J. Solid State Chem. **177**, 139 (2004).

[44] H. Zhou, T.-J. Park, and S. S. Wong, J. Mater. Res. **21**, 2941 (2011).

[45] S. J. Henderson, O. Shebanova, A. L. Hector, P. F. McMillan, and M. T. Weller, Chem. Mater. **19**, 1712 (2007).

[46] K. Momma and F. Izumi, J. Appl. Crystallogr. **44**, 1272 (2011).

[47] H. S. Park, K. E. Kweon, H. Ye, E. Paek, G. S. Hwang, and A. J. Bard, J. Phys. Chem. C **115**, 17870 (2011).

[48] S. Murugesan, M. N. Huda, Y. Yan, M. M. Al-Jassim, and V. (Ravi) Subramanian, J. Phys. Chem. C **114**, 10598 (2010).

[49] W. L. Liu, H. R. Xia, H. Han, and X. Q. Wang, J. Mater. Sci. **40**, 1827 (2005).

[50] S. Gupta and V. R. Subramanian, ACS Appl. Mater. Interfaces **7**, (2014).

[51] Q. Fu, T. He, J. L. Li, and G. W. Yang, J. Appl. Phys. **111**, 124306 (2012).

[52] A. Salamat, A. L. Hector, P. F. McMillan, and C. Ritter, Inorg. Chem. **50**, 11905

(2011).

[53] S. Gupta, L. De Leon, and V. R. Subramanian, Phys. Chem. Chem. Phys. **16**, 12719 (2014).

[54] W. Yao, H. Wang, X. H. Xu, J. T. Zhou, X. N. Yang, Y. Zhang, and S. X. Shang, Appl. Catal. A Gen. **259**, 29 (2004).

[55] J. K. Park, C. H. Kim, K. J. Choi, H. D. Park, and S. Y. Choi, J. Mater. Res. **16**, 2568 (2001).

[56] J. M. Sohn, M. R. Kim, and S. I. Woo, Catal. Today **83**, 289 (2003).

[57] S. S. Kim and W.-J. Kim, J. Cryst. Growth **281**, 432 (2005).

[58] R. D. Shannon and C. T. Prewitt, Acta Crystallogr. Sect. B **26**, 1046 (1970).

[59] R. D. Shannon and C. T. Prewitt, Acta Crystallogr. Sect. B **25**, 925 (1969).

[60] R. D. Shannon, Acta Crystallogr. Sect. A **32**, 751 (1976).

[61] M. A. Subramanian, G. Aravamudan, and G. V. Subba Rao, Prog. Solid State Chem. **15**, 55 (1983).

[62] R. Seshadri, Solid State Sci. **8**, 259 (2006).

[63] A. P. Ramirez, A. Hayashi, R. J. Cava, R. Siddharthan, and B. S. Shastry, Nature **399**, 333 (1999).

[64] B. Canals and C. Lacroix, Phys. Rev. Lett. **80**, 2933 (1998).

[65] A. P. Ramirez, Annu. Rev. Mater. Sci. **24**, 453 (1994).

[66] D. P. Shoemaker, R. Seshadri, A. L. Hector, A. Llobet, T. Proffen, and C. J. Fennie, Phys. Rev. B - Condens. Matter Mater. Phys. **81**, 144113 (2010).

[67] J. Cagnon, D. S. Boesch, N. H. Finstrom, S. Z. Nergiz, S. P. Keane, and S. Stemmer, J. Appl. Phys. **102**, 044102 (2007).

[68] D. P. Shoemaker, R. Seshadri, M. Tachibana, and A. L. Hector, Phys. Rev. B - Condens. Matter Mater. Phys. **84**, 064117 (2011).

[69] J. Hou, R. V. Kumar, Y. Qu, and D. Krsmanovic, Scr. Mater. **61**, 664 (2009).

[70] H. Yan, H. Zhang, Z. Zhang, R. Ubic, and M. J. Reece, J. Eur. Ceram. Soc. **26**, 2785 (2006).

[71] M. Catti, G. Valerio, and R. Dovesi, Phys. Rev. B **51**, 7441 (1995).

[72] D. W. Hwang, H. G. Kim, J. S. Lee, J. Kim, W. Li, and S. H. Oh, J. Phys. Chem. B **109**, 2093 (2005).

[73] H. K. Schmid and W. Mader, Micron **37**, 426 (2006).

[74] D. K. Zhong, J. Sun, H. Inumaru, and D. R. Gamelin, J. Am. Chem. Soc. **131**, 6086 (2009).

[75] M. N. Huda, A. Walsh, Y. Yan, S.-H. Wei, and M. M. Al-Jassim, J. Appl. Phys. **107**, 123712 (2010).

[76] A. Bhaumik, A. M. Shearin, R. Patel, and K. Ghosh, Phys. Chem. Chem. Phys. **16**, 11054 (2014).

[77] T. Grewe, K. Meier, and H. Tüysüz, Catal. Today **225**, 142 (2014).

[78] G. Zhu, M. Hojamberdiev, W. Que, and P. Liu, Ceram. Int. **39**, 9163 (2013).

[79] X. Wang, R. Zheng, Z. Liu, H.-P. Ho, J. Xu, and S. P. Ringer, Nanotechnology **19**, 455702 (2008).

[80] M. Hojamberdiev, K. Katsumata, K. Morita, S. A. Bilmes, N. Matsushita, and K. Okada, Appl. Catal. A Gen. **457**, 12 (2013).

[81] A. I. Gubanov, E. S. Dedova, P. E. Plyusnin, E. Y. Filatov, T. Y. Kardash, S. V. Korenev, and S. N. Kulkov, Thermochim. Acta **597**, 19 (2014).

[82] Y. Shen, M. Huang, Y. Huang, J. Lin, and J. Wu, J. Alloys Compd. **496**, 287 (2010).

[83] Y.-H. Li, J.-F. Huang, J.-Y. Li, L.-Y. Cao, J. Lu, and J.-P. Wu, Mater. Lett. **135**, 168 (2014).

[84] H. Zhang, M. Lü, S. Liu, X. Song, Y. Zhou, Z. Xiu, Z. Qiu, A. Zhang, and Q. Ma, Thin Solid Films **517**, 764 (2008).

[85] T. Kidchob, L. Malfatti, D. Marongiu, S. Enzo, and P. Innocenzi, J. Am. Ceram. Soc. **93**, 2897 (2010).

[86] H. Wang, H. H. Chen, H. Borrmann, Z. J. Zhang, and J. T. Zhao, J. Alloys Compd. **545**, 135 (2012).

[87] H. Peng, C. K. Chan, S. Meister, X. F. Zhang, and Y. Cui, Chem. Mater. **21**, 247 (2009).

[88] S. Ikeda, M. Fubuki, Y. K. Takahara, and M. Matsumura, Appl. Catal. A Gen. **300**, 186 (2006).

[89] W. Ma, Z. Li, and W. Liu, Ceram. Int. **41**, 4340 (2015).

[90] P. Bowen and C. Carry, Powder Technol. **128**, 248 (2002).

[91] Y. Tian, L. Zhang, and J. Zhang, J. Alloys Compd. **537**, 24 (2012).

[92] M. Ratova, G. T. West, and P. J. Kelly, Vacuum **115**, 66 (2015).

[93] N. Mahato, A. Banerjee, A. Gupta, S. Omar, and K. Balani, Prog. Mater. Sci. (2015).

[94] K. Maeda, J. Photochem. Photobiol. C Photochem. Rev. **12**, 237 (2011).

[95] A. Kudo and Y. Miseki, Chem. Soc. Rev. **38**, 253 (2009).

[96] T. W. Kim, Y. Ping, G. A. Galli, and K.-S. Choi, Nat. Commun. **6**, 8769 (2015).

[97] J. a. Schwarz, C. Contescu, and A. Contescu, Chem. Rev. **95**, 477 (1995).

[98] W. Feng Yao, H. Wang, X. Hong Xu, Y. Zhang, X. Na Yang, S. Xia Shang, Y. Hui Liu, J. Tao Zhou, and M. Wang, J. Mol. Catal. A Chem. **202**, 305 (2003).

[99] F. E. Osterloh, Chem. Mater. **20**, 35 (2008).

[100] W. Yao, H. Wang, X. H. Xu, J. T. Zhou, X. N. Yang, Y. Zhang, and S. X. Shang, Appl. Catal. A Gen. **259**, 29 (2004).

[101] L. Z. Pei, H. D. Liu, N. Lin, and H. Y. Yu, J. Alloys Compd. **622**, 254 (2015).

[102] R. G., S. Palla, N. K. Veldurthi, R. J.R., H. P. a., and V. M., Int. J. Hydrogen Energy **39**, 15352 (2014).

[103] K. Su, Z. Ai, and L. Zhang, J. Phys. Chem. C **116**, 17118 (2012).

[104] S. Murugesan, M. N. Huda, Y. Yan, M. M. Al-Jassim, and V. (Ravi) Subramanian, J. Phys. Chem. C **114**, 10598 (2010).

[105] C. Enache, J. Schoonman, and R. Van Krol, J. Electroceramics **2**, 177 (2004).

[106] W. Choi, A. Termin, and M. R. Hoffmann, J. Phys. Chem. **98**, 13669 (1994).

[107] B. J. Morgan and G. W. Watson, Phys. Rev. B - Condens. Matter Mater. Phys. **80**, 2 (2009).

[108] M. Ni, M. K. H. Leung, D. Y. C. Leung, and K. Sumathy, Renew. Sustain. Energy Rev. **11**, 401 (2007).

[109] S. Murugesan and V. R. Subramanian, Chem. Commun. (Camb). 5109 (2009).

[110] F. Glas, J. Appl. Phys. **108**, 073506 (2010).

[111] O. Gunawan and S. Guha, Sol. Energy Mater. Sol. Cells **93**, 1388 (2009).

[112] M. Fabrizio and V. Berti, **123**, 109 (2011).

[113] P. Cheyssac, M. Sacilotti, and G. Patriarche, J. Appl. Phys. **100**, 044315 (2006).

[114] V. a. Nebol'sin, a. a. Shchetinin, a. a. Dolgachev, and V. V. Korneeva, Inorg. Mater. **41**, 1256 (2005).

[115] S. Christiansen, R. Schneider, R. Scholz, U. Gösele, T. Stelzner, G. Andrä, E. Wendler, and W. Wesch, J. Appl. Phys. **100**, 084323 (2006).

[116] X. Y. Chen, Z. J. Zhang, and S. W. Lee, J. Solid State Chem. **181**, 166 (2008).

[117] A. Wosylus, S. Hoffmann, M. Schmidt, and M. Ruck, Eur. J. Inorg. Chem. 1469 (2010).

[118] A. Mishra and K. N. Tandon, Inorg. Chem. **10**, 1896 (1971).

[119] J. Hou, R. Cao, Z. Wang, S. Jiao, and H. Zhu, J. Mater. Chem. **21**, 7296 (2011).

[120] T. Liu, P. Rao, and I. M. C. Lo, Sci. Total Environ. **407**, 3407 (2009).

[121] M. C. Biesinger, B. P. Payne, A. P. Grosvenor, L. W. M. Lau, A. R. Gerson, and R. S. C. Smart, Appl. Surf. Sci. **257**, 2717 (2011).

[122] G. P. Halada, J. Electrochem. Soc. **138**, 2921 (1991).

[123] A. Lahmar, K. Zhao, S. Habouti, M. Dietze, C.-H. Solterbeck, and M. Es-Souni, Solid State Ionics **202**, 1 (2011).

[124] P. Ravindran, R. Vidya, A. Kjekshus, H. Fjellvåg, and O. Eriksson, Phys. Rev. B **74**, 224412 (2006).

[125] J.-Y. Choi, C.-H. Choi, K.-H. Cho, T.-G. Seong, S. Nahm, C.-Y. Kang, S.-J. Yoon, and J.-H. Kim, Acta Mater. **57**, 2454 (2009).

[126] M. C. Fravventura, L. D. a. Siebbeles, and T. J. Savenije, J. Phys. Chem. C **118**, 7337 (2014).

[127] X. Ma, Y. Dai, M. Guo, and B. Huang, Langmuir **29**, 13647 (2013).

[128] M. Ni, M. K. H. Leung, D. Y. C. Leung, and K. Sumathy, Renew. Sustain. Energy Rev. **11**, 401 (2007).

[129] M. Nolan, A. Iwaszuk, and K. A. Gray, J. Phys. Chem. C **118**, 27890 (2014).

[130] B. D. Alexander, P. J. Kulesza, I. Rutkowska, R. Solarska, and J. Augustynski, J. Mater. Chem. **18**, 2298 (2008).

[131] D. Zhang, M. Yang, and S. Dong, J. Phys. Chem. C **119**, 1451 (2015).

[132] T. Sekiya, A. Tzuzuki, S. Kawakami, Y. Torii, N. Tsuboi, and T. Futakuchi, J. Mater. Sci. **23**, 3300 (1988).

[133] S. Moser, L. Moreschini, J. Jaćimović, O. S. Barišić, H. Berger, A. Magrez, Y. J. Chang, K. S. Kim, A. Bostwick, E. Rotenberg, L. Forró, and M. Grioni, Phys. Rev. Lett. **110**, 1 (2013).

[134] G. Shao, J. Phys. Chem. C **113**, 6800 (2009).

[135] Y. Wu, G. Lu, and S. Li, J. Phys. Chem. C 9950 (2009).

[136] Z. Bian, J. Zhu, S. Wang, Y. Cao, X. Qian, and H. Li, J. Phys. Chem. C **112**, 6258 (2008).

[137] Q. Fu, T. He, J. L. Li, G. W. Yang, H. Zhou, T. Park, J. Zeng, H. Wang, Y. Zhang, J. Wang, Z. Zou, J. Ye, R. Abe, M. Higashi, K. Sayama, and Y. Abe, J. Appl. Phys. **111**, 124306 (2012).

[138] H. T. Sui, D. M. Yang, H. Jiang, Y. L. Ding, and C. H. Yang, Ceram. Int. **39**, 1125 (2013).

[139] S. Gupta and V. R. Subramanian, ACS Appl. Mater. Interfaces **7**, DOI: 10.1021/am503396r (2014).

[140] C. L. Mayfield, V. (Ravi) Subramanian, and M. N. Huda, J. Phys. Condens. Matter **27**, 315502 (2015).

[141] M. Ni, M. K. H. Leung, D. Y. C. Leung, and K. Sumathy, Renew. Sustain. Energy Rev. **11**, 401 (2007).

[142] R. a. Marcus, Angew. Chemie Int. Ed. **32**, 1111 (1993).

[143] R. a. Marcus and N. Sutin, Biochim. Biophys. Acta - Rev. Bioenerg. **811**, 265 (1985).

[144] T. Holstein, Ann. Phys. (N. Y). **8**, 325 (1959).

[145] T. Holstein, Ann. Phys. (N. Y). **8**, 343 (1959).

[146] L. Friedman and T. Holstein, Ann. Phys. (N. Y). **21**, 494 (1963).

[147] D. Emin and T. Holstein, Ann. Phys. (N. Y). **53**, 439 (1969).

[148] D. Emin and T. Holstein, Phys. Rev. Lett. **36**, 323 (1976).

[149] I. G. Austin and N. F. Mott, Adv. Phys. **18**, 41 (1969).

[150] G. Kresse and D. Joubert, Phys. Rev. B **59**, 11 (1999).

[151] B. J. Morgan and G. W. Watson, Surf. Sci. **601**, 5034 (2007).

[152] N. Deskins and M. Dupuis, Phys. Rev. B **75**, 195212 (2007).

[153] K. E. Kweon and G. S. Hwang, Phys. Rev. B **87**, 205202 (2013).

[154] A. J. E. Rettie, H. C. Lee, L. G. Marshall, J. F. Lin, C. Capan, J. Lindemuth, J. S. McCloy, J. Zhou, A. J. Bard, and C. B. Mullins, J. Am. Chem. Soc. **135**, 11389 (2013).

[155] K. E. Kweon, G. S. Hwang, J. Kim, S. Kim, and S. Kim, Phys. Chem. Chem. Phys. **17**, 256 (2015).

Biographical Information

Cedric Mayfield obtained his MS and PhD in physics from the University of Texas Arlington in 2013 and 2015. For his thesis work, under M.N. Huda, he provided the first electronic structure explanation for the preference of Au catalysts in Si nanostructure growth. His present work with M.N. Huda concerns the application of electronic structure theory to photoelectrochemical hydrogen production of mixed metal oxide photocatalysts. His focus has been on stability and conduction properties of a multi metal oxide. For his efforts he has been awarded by the Annual Electronic Structure Theory Workshop and American Physical Society in 2014 and 2015.